remote sensing

MDPI

Article

Pressure-Related Discrepancies in Landsat 8 Level 2 Collection 2 Surface Reflectance Products and Their Correction

Santosh Adhikari, Larry Leigh * and Dinithi Siriwardana Pathiranage

Image Processing Laboratory, Engineering Office of Research, South Dakota State University (SDSU), Brookings, SD 57007, USA; santosh.adhikari@jacks.sdstate.edu (S.A.); dinithi.siriwardanapathiranage@sdstate.edu (D.S.P.)

* Correspondence: larry.leigh@sdstate.edu; Tel.: +1-605-688-4161

Abstract: Landsat 8 Level 2 Collection 2 (L2C2) surface reflectance (SR) products are widely used in various scientific applications by the remote sensing community, where their accuracy is vital for reliable analysis. However, discrepancies have been observed at shorter wavelength bands, which can affect certain applications. This study investigates the root cause of these differences by analyzing the assumptions made in the Land Surface Reflectance Code (LaSRC), the atmospheric correction algorithm of Landsat 8, as currently implemented at United States Geological Survey Earth Resources Observation and Science (USGS EROS), and proposes a correction method. To quantify these discrepancies, ground truth SR measurements from the Radiometric Calibration Network (RadCalNet) and Arable Mark 2 sensors were compared with the Landsat 8 SR. Additionally, the surface pressure measurements from RadCalNet and the National Centers for Environmental Information (NCEI) were evaluated against the LaSRC-calculated surface pressure values. The findings reveal that the discrepancies arose from using a single scene center surface pressure for the entire Landsat 8 scene pixels. The pressure-related discrepancies were most pronounced in the coastal aerosol and blue bands, with greater deviations observed in regions where the elevation of the study area differed substantially from the scene center, such as Railroad Valley Playa (RVUS) and Baotao Sand (BSCN). To address this issue, an exponential correction model was developed, reducing the mean error in the coastal aerosol band for RVUS from 0.0226 to 0.0029 (about two units of reflectance), which can be substantial for dark vegetative and water targets. In the blue band, there is a smaller improvement in the mean error, from 0.0095 to −0.0032 (about half a unit of reflectance). For the green band, the reduction in error was much less due to the significantly lesser impact of aerosol on this band. Overall, this study underscores the need for a more precise estimation of surface pressure in LaSRC to enhance the reliability of Landsat 8 SR products in remote sensing applications.

Keywords: Landsat 8; Level 2; surface reflectance; shorter wavelength bands; LaSRC; scene center; surface pressure; RadCalNet; Arable Mark 2; exponential model

check for updates

Academic Editor: Jian Xu

Received: 8 March 2025
Revised: 1 May 2025
Accepted: 8 May 2025
Published: 9 May 2025

Citation: Adhikari, S.; Leigh, L.; Pathiranage, D.S. Pressure-Related Discrepancies in Landsat 8 Level 2 Collection 2 Surface Reflectance Products and Their Correction. *Remote Sens.* **2025**, *17*, 1676. https://doi.org/10.3390/rs17101676

Copyright: © 2025 by the authors. Licensee MDPI, Basel, Switzerland. This article is an open access article distributed under the terms and conditions of the Creative Commons Attribution (CC BY) license (https://creativecommons.org/licenses/by/4.0/).

1. Introduction

1.1. Background

Earth Observing (EO) satellite sensors are vital tools for capturing images of various landscapes on Earth, facilitating wide-ranging research and analysis of the Earth's land, seas, and atmosphere. The imagery acquired from EO satellites is employed in a wide range of applications, including climate and weather prediction [1], crop monitoring [2],

disease detection and prevention [3], as well as tracking wildfires [4], volcanic activity [5], and atmospheric pollutants [6].

The electromagnetic radiation (EMR) recorded by the EO satellite sensor does not represent the true ground-emitted radiance. Instead, it is a mixture of radiation from the Earth's surface and diffuse sky irradiance resulting from complex interactions with the atmosphere. As EMR travels, it first interacts with the atmosphere, then with the Earth's surface, and finally with the atmosphere again before reaching the sensor. This transmission pathway of EMR introduces atmospheric scattering and interference, altering the direct radiance and distorting the real view of ground conditions.

EO satellite products, specifically Landsat 8 (L8), address these atmospheric complexities through two main processing levels: Level 1 and Level 2. The Level 1 product, which is commonly referred to as top-of-atmosphere (TOA), is available in two correction levels: Level 1 Systematic Terrain (Corrected) (L1GT) and Level 1 Precision Terrain (Corrected) (L1TP), which differ in their application of radiometric, geometric, and precision corrections [7]. Though TOA products include atmospheric effects, potentially distorting the observed target's true characteristics, they offer foundational data for users who require minimal correction or focus on atmospheric phenomena.

On the other hand, the Level 2 Surface Reflectance (SR) product is generated by correcting the Level 1 products for atmospheric effects [8]. The Level 1 product undergoes a complex atmospheric correction algorithm, namely the Land Surface Reflectance Code (LaSRC) [9], which is designed to model the atmospheric conditions at the time of the satellite's overpass, utilizing ancillary data such as ozone levels, water vapor content, carbon dioxide, aerosol distribution, and surface pressure. As SR products aim to correct atmospheric interference, they are expected to represent the surface features of the target more accurately than the TOA product. SR products are preferred by users in the remote sensing community since they require minimal post-processing [10], eliminate the need for custom atmospheric correction, and represent the true nature of the target.

1.2. Issues in Surface Reflectance Products

The increasing preference for Surface Reflection (SR) products highlights the need to address accuracy concerns that may arise from their use. Uncertainties and errors in SR products not only impact the products' accuracy but also propagate through their applications, potentially leading to misleading results and interpretations. Thus, it is imperative to resolve such concerns as swiftly as possible to maintain the reliability of these products.

One notable issue has been identified in the shorter wavelengths (coastal aerosol (CA) and blue bands) of Landsat 8; when compared with ground-based measurements, the SR products from Landsat 8 show deviations, particularly in these bands [11]. Moe et al. discovered in their study that surface reflectance retrieval at CA was troublesome since it exhibited the highest RMSE of 13.6% [12]. Such discrepancies in shorter wavelengths have been consistently reported in conferences and scientific meetings worldwide, underscoring the urgency of the problem. Failure to resolve this issue will likely have significant implications for future Landsat missions, especially given the planned introduction of the violet band [13], which is likely to be similarly affected. These discrepancies have primarily been attributed to the difficulty in accurate estimation of aerosol concentrations, although a detailed study on the impact of aerosol concentrations had not been conducted and was incomplete.

1.3. Challenges

Atmospheric correction remains one of the most challenging facets of remote sensing, primarily due to the inherent complexity of accurately assessing atmospheric conditions during satellite overpasses. Various correction methods have been developed to tackle these challenges, which can primarily be divided into physics-based and image-based methods [14]. Physical methods, though complex, are the most accurate methods and require auxiliary data such as aerosol optical depth (AOD), aerosol type, ozone concentration, water vapor, as well as sensor and solar zenith and azimuth angles [14], the estimation of which on a global scale is an exceptionally complicated task. Examples of physical methods include 6SV (vector version of the Second Simulation of the Satellite Signal in the Solar Spectrum) [15,16], 5S (Simulation of the Satellite Signal in the Solar Spectrum) [17], MODTRAN (MODerate resolution atmospheric TRANsmission) [18], and LOWTRAN [19]. These methods are now being integrated as foundational approaches within new atmospheric correction techniques, such as the LaSRC [9], Landsat Ecosystem Disturbance Adaptive Processing System (LEDAPS) [20], Py6S [21], Framework for Operational Radiometric Correction for Environmental monitoring (FORCE) [22], OPERA [23], and Fast Line-of-sight Atmospheric Analysis of Spectral Hypercubes (FLAASH) [24].

In contrast to the data-intensive physical methods, image-based methods are relatively simpler and rely on image metadata for SR estimation [25]. Some of the most widely used image-based methods are the Empirical Line Method (ELM) [26], Dark Object Subtraction (DOS) [27], and histogram matching [28].

Estimating AOD and aerosol types during satellite passage remains a key challenge for physical methods because of their temporal and spatial variability. To address this, advancements such as enhancements to the Deep Blue algorithm [29] have led to improved aerosol model selection and surface reflectance estimation, supporting more accurate MODIS aerosol products [30]. Additionally, NASA's dark target algorithm [31,32] continues to undergo modifications with the aim of better characterizing aerosol systems [33].

During atmospheric correction, algorithms often make simplifying assumptions due to complexities in estimating the atmospheric parameters or computational limitations. For example, LaSRC (version 1.5.0) uses a single scene center value for surface pressure, ozone, and water vapor across all scene pixels. Additionally, a 3×3 pixel window is used to estimate AOD. The effect of assuming the single scene center ozone and water vapor could create the issue in SR products, but that needs further research and investigation and is not the scope of this paper. However, the assumptions related to surface pressure (use of scene center surface pressure for the entire scene pixels) affect the surface reflectance, which is discussed in this paper.

1.4. Research Objective

In LaSRC, surface pressure plays a critical role in estimating intrinsic atmospheric reflectance, total atmospheric transmission, spherical albedo, gaseous transmission, and Rayleigh scattering reflectance, which are the governing factors of atmospheric correction. Therefore, incorrect surface pressure estimates can substantially alter the surface reflectance products. This research aims to explore in greater detail the process of surface pressure estimation within LaSRC, assess its impact on Landsat 8 Level 2 Collection 2 (L2C2) surface reflectance accuracy, and propose short-term solutions to mitigate the effects of pressure-related inaccuracies. This study underscores the importance of accurate surface pressure estimation apart from aerosol concentrations within LaSRC, especially for the shorter wavelength bands, to ensure the reliability of Landsat 8 SR products.

2. Materials

2.1. Study Areas

In this study, the Landsat 8 L2C2 surface reflectance product was compared with the in situ surface reflectance measurements made at four Radiometric Calibration Network (RadCalNet) [34] sites and four South Dakota State University (SDSU) sites located at Brookings and Arlington, South Dakota. This section presents a detailed overview of the sites used in this research.

2.1.1. RadCalNet Site—Railroad Valley Playa

RadCalNet is a global network of calibration sites established by the Infrared Visible Optical Sensors (IVOS), which is a subgroup of the Committee on Earth Observation Satellites (CEOS) Working Group on Calibration and Validation (WGCV) [34]. It was formed to support the calibration and validation of satellite sensors by offering globally consistent data and improved temporal sampling through automated, SI-traceable instrumentation. The data can be accessed through the RadCalNet website at [35]. Currently, there are five sites under RadCalNet: Railroad Valley Playa in the US, La Crau in France, Gobabeb in Namibia, and two sites in Baotao, China.

Railroad Valley Playa, located in Nevada, US (RVUS), is a longstanding radiometric calibration site maintained by the University of Arizona. The site has been used for radiometric calibration since 1996 and represents an area of 1 km^2 (1 km $\times$ 1 km). It is centered at 38.497°N and 115.690°W at an altitude of 1435 m above sea level [36]. The average surface reflectance is characteristic of clay-based playas and generally stable under dry conditions but varies during periodic snowfall and rainfall events [34]. The site is generally flat with less than 3 m elevation variation over the Region of Interest (ROI). However, it is surrounded by mountains as high as 2000 m above the playa's surface. The surface reflectance variability across the site is 1.5% for the ROI of 1000 $\times$ 1000 m^2 [36]. In this study, the RVUS site ROI of 32 $\times$ 32 pixels was used for the SR calculation of the Landsat image. Figure 1a shows the Landsat 8 RGB composite band (Band 4, 3, 2) over RVUS with ROI denoted by a red box, and Figure 1b shows the site view from the ground.

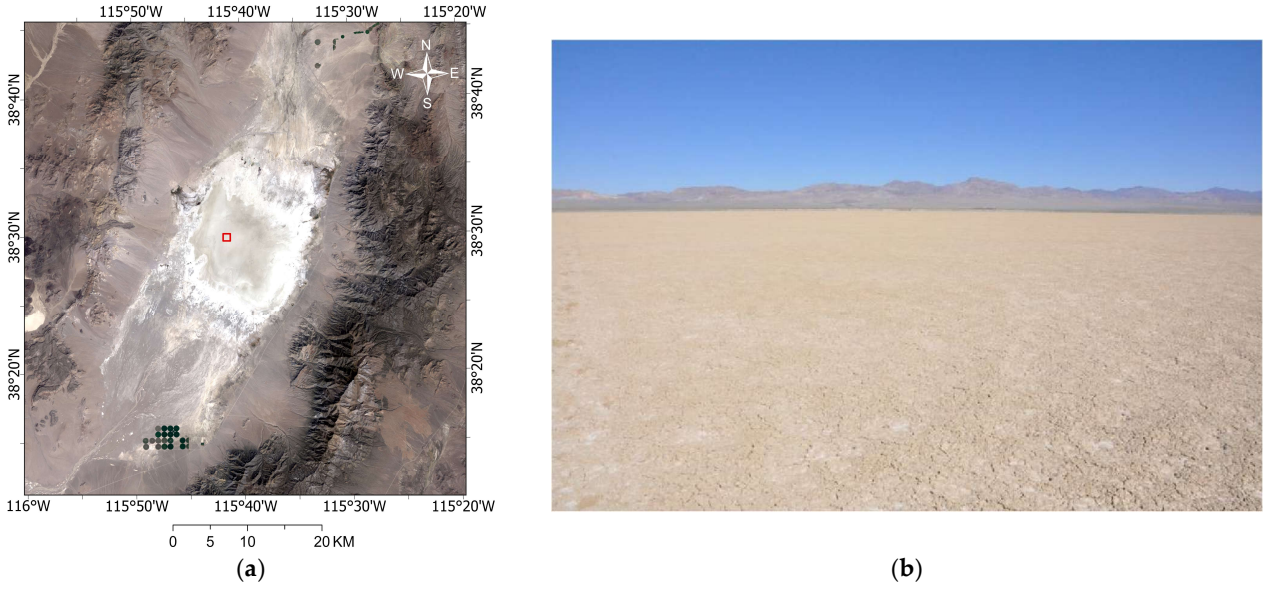
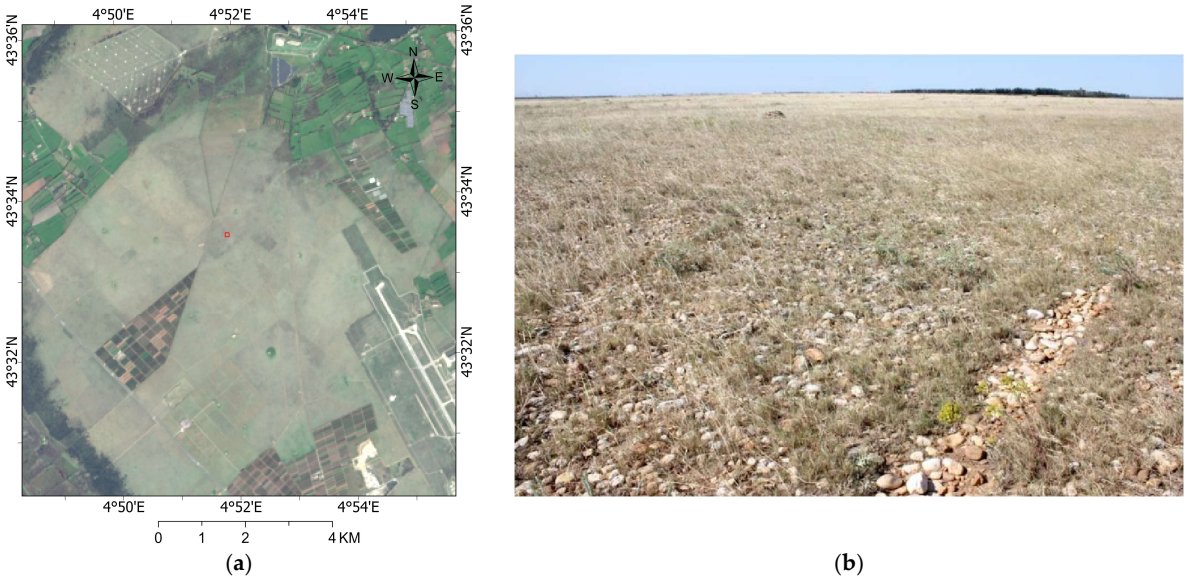


Figure 1. (**a**) True color image of RVUS (red box denotes the site ROI) imaged by Landsat 8 on 25 September 2024. (**b**) Site view from the ground [36].

2.1.2. RadCalNet Site—La Crau

La Crau (LCFR), located in southeastern France, is a traditional vicarious calibration site that has been operational since 1987 [37]. The site is operated and maintained by the French Space Agency, Center National d'Études Spatiales (CNES), and lies within the Reserve Naturelle des Coussouls de Crau. Its geographical coordinates are 43.558950°N and 4.864361°E, and it is situated at an elevation of 20 m above sea level. The site contains a thin layer of pebbly soil with sparse vegetation cover. RadCalNet reflectance spectra are representative of a disk with a radius of 30 m. The surface reflectance variability across a 100 × 100 m^2 region is approximately 3% [38]. In this study, the LCFR site ROI of 3 × 3 pixels was used for the SR calculation of the Landsat image. Figure 2a shows the Landsat 8 RGB composite band image over LCFR with the ROI denoted by a red box, and Figure 2b shows the site view from the ground.



(**a**) (**b**)

Figure 2. (**a**) True color image of LCFR (red box denotes the site ROI) imaged by Landsat 8 on 1 November 2024. (**b**) Site view from the ground [38].

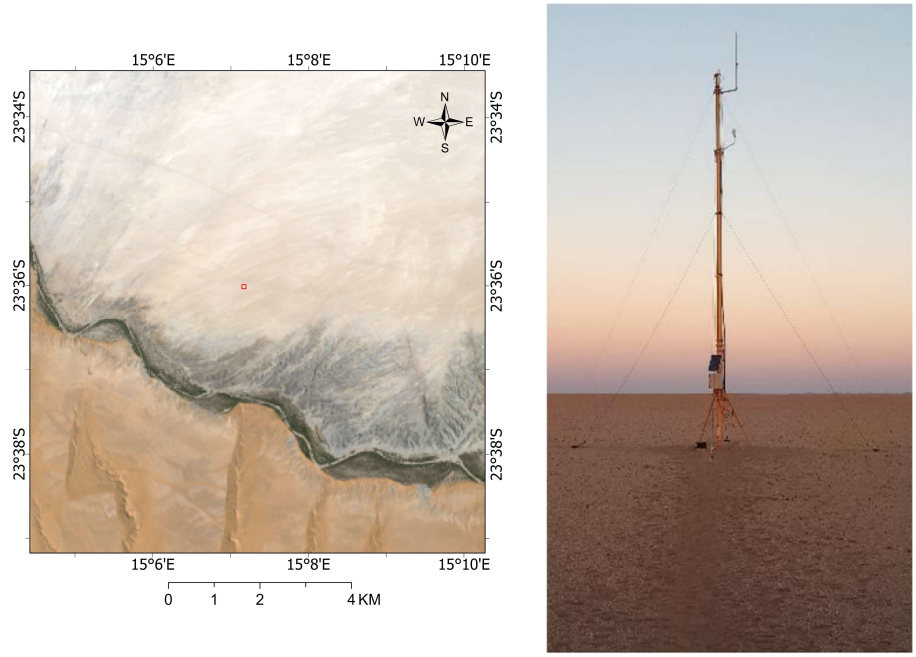
2.1.3. RadCalNet Site—Gobabeb

Gobabeb (GONA), located in Namibia, was established in July 2017 through a joint venture between the European Space Agency (ESA) and CNES. The site is now operated and maintained by the National Physical Laboratory (NPL) in the UK. It lies within the Namib-Naukluft National Park at coordinates 23.600200°S and 15.119561°E, with an altitude of 510 m above sea level. The RadCalNet reflectance spectra are representative of a disk with a radius of 30 m. The site features sandy and gravelly terrain, characteristic of an arid desert environment. Surface reflectance variability across a 100 × 100 m^2 region ranges from 3% to 5% [39]. In this study, the GONA site ROI of 3 × 3 pixels was used for the SR calculation of the Landsat image. Figure 3a shows the Landsat 8 RGB composite band image over GONA with the ROI denoted by a red box, and Figure 3b shows the site view from the ground.

2.1.4. RadCalNet Site—Baotao Sand

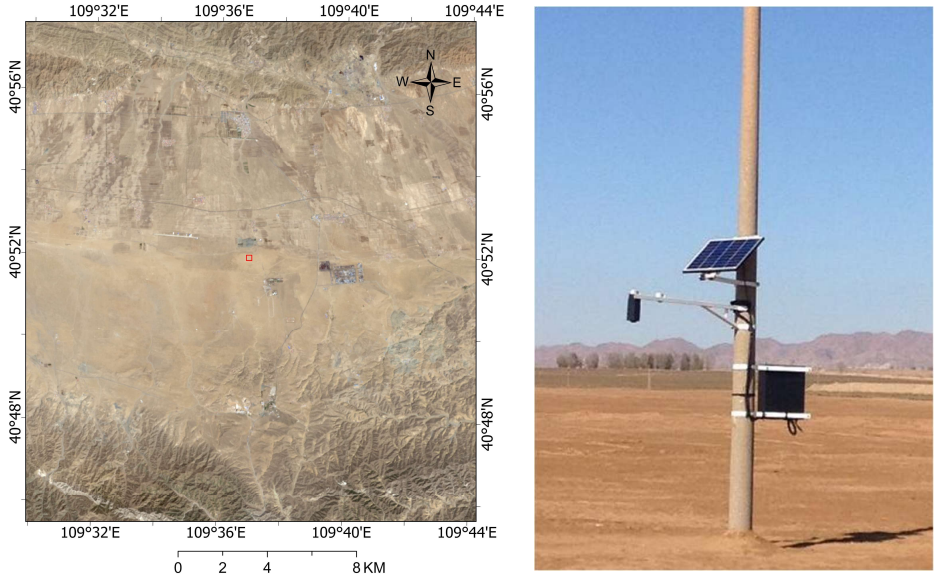
Baotao Sand is a radiometric and geometric calibration test site located at Urad Qianqi, Inner Mongolia, in northern China, and has been a part of RadCalNet since 2020. It is operated and maintained by the Chinese Academy of Science. The site features two types of targets for vicarious radiometric calibration: three permanent artificial targets (BTCN) designed for airborne and high spatial resolution sensors and a large sandy desert target

(BSCN) suited for moderate spatial resolution sensors like Landsat. BSCN is approximately 1.8 km northwest of BTCN. This study utilizes RadCalNet measurements from the BSCN target, centered at 40.8658°N and 109.6155°E, at an altitude of 1270 m above sea level. The RadCalNet spectral reflectance measurements from BSCN represent a square area of 300 × 300 m^2. Surface reflectance variability across this site is less than 3% across almost all wavelengths for the 300 × 300 m^2 region [41]. In this study, the BSCN site ROI of 8 × 8 pixels was used for the SR calculation of the Landsat image. Figure 4a shows the Landsat 8 RGB composite band image over BSCN with the ROI denoted by a red box, and Figure 4b shows the site view from the ground.



(**a**) (**b**)

Figure 3. (**a**) True color image of GONA (red box denotes the site ROI) imaged by Landsat 8 on 9 October 2024. (**b**) Site view from the ground [40].



(**a**) (**b**)

Figure 4. (**a**) True color image of BSCN (red box denotes the site ROI) imaged by Landsat 8 on 13 May 2024. (**b**) Site view from the ground [41].

2.1.5. South Dakota State University—SDSU Sites

The Image Processing Laboratory at South Dakota State University (SDSU IP Lab) conducts research on EO satellites, focusing on their radiometric, geometric, and spatial characterization, as well as correction, calibration, and validation to assess their performance [42]. Recently, the usual in-person vicarious calibration performed by the SDSU IP Lab has been extended to the use of Arable Mark 2 Sensors, which are low-cost and automated radiometers that can be used in the validation of Level 2 products of satellite sensors like Landsat 8 [43]. In this study, measurements taken by Arable Mark 2 sensors at four SDSU IP Lab sites—two sites in Brookings (Research Park and North Airport) and two sites in Arlington, South Dakota (soybean/corn and grass farms)—from 2020 to 2023 have been used in the comparison of SR with the Landsat 8 measurements. Table 1 shows detailed information about the Arable Mark 2 deployed sites used in this study.

Table 1. Information about the Arable Mark 2 deployed sites used in this study.

Arable Mark 2 Sites	Center Latitude/Longitude	Land Cover	ROI Size (m)
Research Park	44°19′16.21″N 96°45′43.08″W	Alfalfa	60 × 90
North Airport	44°19′26.78″N 96°49′25.43″W	Grass	90 × 60
Arlington	44°24′37.42″N 97°7′39.40″W	Grass	90 × 30
Arlington	44°24′38.76″N 97°7′31.90″W	Soybean/Corn	60 × 60

2.2. Atmospheric Parameters

Physics-based atmospheric correction methods rely on accurately characterizing and compensating for the effects of various atmospheric components to derive accurate SR products from TOA products. In LaSRC, atmospheric parameters, aerosols, absorbing gases (ozone, water vapor, oxygen, and carbon dioxide), and surface pressure are used in the correction process. These parameters collectively help to model the atmosphere at the time of satellite overpass so as to account for their effects on the TOA products.

2.2.1. Aerosols

Aerosols are tiny particles (ranging from 10^{-4} to 10 microns in radius) suspended in the atmosphere, which have impacts on solar radiation, human health, and ecological systems. The optical properties of aerosols are spectrally dependent and are characterized by parameters such as aerosol optical depth, angular scattering phase function, and single scattering albedo, which are determined by factors like particle size distribution, shape, chemical composition, and refractive indices [44]. These complexities introduce challenges in the accurate modeling of aerosol effects in atmospheric correction. Moreover, diverse types of aerosol models (urban, rural, continental, maritime, and others) add another layer of difficulty. Since these models vary by location and season, estimating the absorption and scattering effects of aerosols becomes an even more convoluted process.

2.2.2. Absorbing Gases

Although most spectral bands of satellite sensors are designed to operate within atmospheric windows, some bands inevitably overlap with absorption regions of the gases. Among these gases, water vapor (H_2O) and ozone (O_3) are the leading contributing gases affecting the absorption of solar radiation. Other gases include carbon dioxide (CO_2) and

oxygen (O_2). The effect of gaseous absorption is spectrally dependent, as it varies with the wavelength.

2.2.3. Rayleigh Scattering

Scattering caused by the gaseous components of the atmosphere is a well-established phenomenon, and it depends upon the surface pressure, wavelengths, and the solar and view angles of the satellite sensors.

2.2.4. Surface Pressure

Surface pressure is used to calculate Rayleigh scattering and trace gas transmission. Moreover, in the LaSRC, it is used to calculate the atmospheric intrinsic reflectance, total atmospheric transmission, and spherical albedo. Thus, accurate surface pressure estimation is crucial for accurately modeling the atmosphere at the time of satellite overpass.

2.3. Landsat 8

Landsat 8, part of the Landsat series of multispectral satellite sensors, was launched on February 11, 2023, through a collaboration between the National Aeronautics and Space Administration (NASA) and the United States Geological Survey (USGS). It features two sensors: the Operational Land Imager (OLI), which operates in the visible, near-infrared (NIR), and shortwave-infrared (SWIR) regions, and the Thermal Infrared Sensor (TIRS), which measures land surface temperatures across two thermal bands. These two sensors provide data across 11 spectral bands: Coastal Aerosol, Blue, Green, Red, NIR, SWIR 1, SWIR 2, Panchromatic, Cirrus, TIRS 1, and TIRS 2. The satellite has a temporal resolution of 16 days, with spatial resolutions of 30 m for optical bands, 15 m for panchromatic, and 100 m for thermal bands. It orbits at an altitude of 705 km and captures data with a swath width of 185 km.

Landsat data are processed into two levels: Level 1 and Level 2. These datasets can be converted from digital numbers (DNs) to physical units using radiometric coefficients provided in metadata files. The Landsat datasets are organized into a tiered collection management structure to ensure consistent data quality and accessibility. To ensure consistent data quality and accessibility, Landsat datasets are managed in a tiered collection structure. Collection 1 (1972–2022) standardized Level-1 products but has been replaced by Collection 2, which introduces improved geolocation accuracy, updated elevation models, enhanced calibration, and global Level-2 surface reflectance and temperature products from 1982 to the present [45]. This study utilizes OLI Level 2 Collection 2 (L2C2) data.

2.4. Arable Mark 2 Sensor

The Arable Mark 2 sensor is a portable, automated, simple, and low-cost radiometer that can be used to validate surface reflectance products of EO satellite sensors [43]. The sensor measures the upwelling and downwelling radiance in seven spectral bands: blue, green, yellow, red, red-edge, NIR-1, and NIR-2, ranging from 420 nm to 965 nm [46]. The surface reflectance can be calculated by taking the ratio of upwelling to downwelling radiance. It has a radiometric range of 0 to 1200 w/m^2 with an accuracy of $\pm 10\%$ [46]. In addition to the radiance measurements, it provides measurements related to climatic variables as well as vegetation indices [47], making it a valuable tool for agricultural applications.

3. Methodology

The overall research methodological framework used in this study is shown in Figure 5. In this work, ground-based surface reflectance data from RadCalNet and Arable were integrated with satellite-based SR from Landsat 8 to investigate how LaSRC's atmospheric correction is affected by variations in surface pressure. The ground measurements were

matched and filtered to Landsat 8 overpass times, and the SR difference (ground truth minus Landsat 8), as well as the surface pressure ratio (scene center pressure estimated by LaSRC over ground-based pressure), were calculated. These quantities served as the basis for analyzing potential biases or systematic errors introduced by LaSRC's uniform pressure assumption. Various weighted regression models, including linear, polynomial, logarithmic, and exponential forms, were then evaluated to capture the relationship between SR difference and surface pressure ratio. Finally, the model with the best performance was validated using RadCalNet data from 2024, which could be used to correct pressure-related discrepancies from LaSRC.

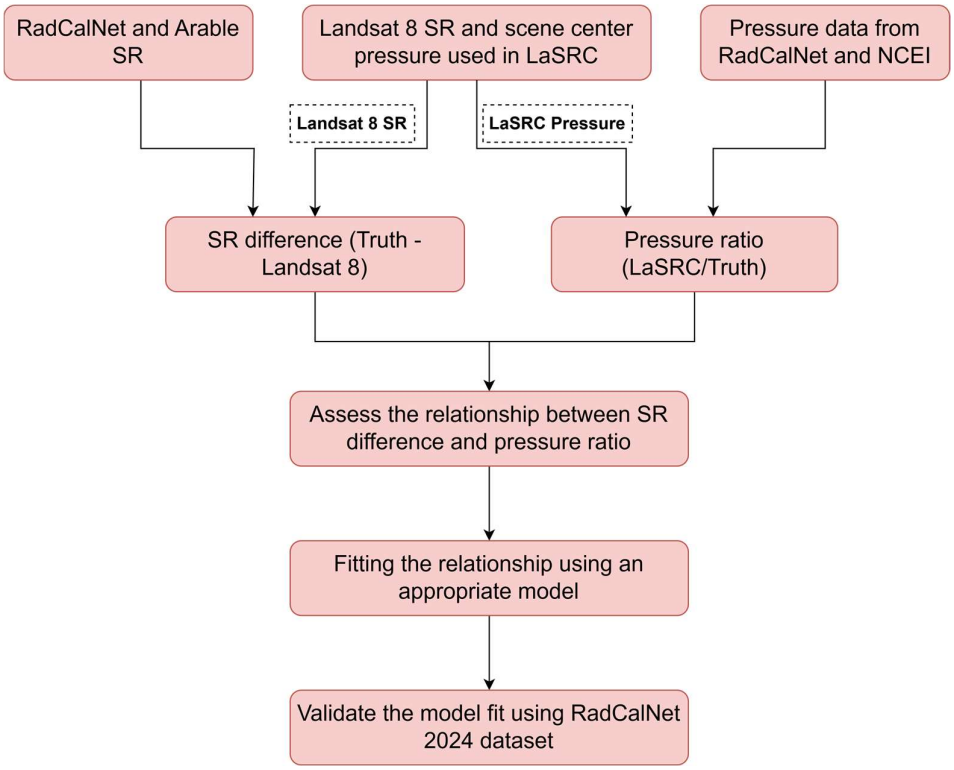


Figure 5. Overall research methodological framework used in this study.

3.1. Land Surface Reflectance Code

Land Surface Reflectance Code, also known as LaSRC, is a physics-based atmospheric correction algorithm used to generate the Landsat 8/9 surface reflectance products. The algorithm was originally developed by Eric F. Vermote at NASA's Goddard Space Flight Center (GSFC) [48] and was written in the FORTRAN programming language. It was later modified by the USGS Earth Resources Observation and Science (EROS) Center and is written in the C programming language. Currently, USGS LaSRC version 1.5.0 is used to derive the SR [48], and all the analysis and discussion carried out in this work are based on the same version. At first, LaSRC generates the TOA reflectance and brightness temperature using the radiometric coefficients from the metadata and then uses the auxiliary datasets, which can be accessed at the USGS web portal [49], to generate the SR product.

3.1.1. Surface Reflectance Inversion in LaSRC

The atmospheric correction method used in LaSRC is based on inverting a simplified equation applicable to the Lambertian surface case, excluding adjacency effects [9]. This approach incorporates a basic coupling of atmospheric gas absorption and scattering by molecules and aerosols, as implemented in the 6SV radiative transfer code [15,50], using Equation (1).

$$\rho_{TOA}\left(\theta_s,\ \theta_v,\ \phi,\ P,\ \overbrace{\tau_A,\ \omega_0,\ P_A}^{Aer},\ U_{H_2O},\ U_{O_3}\right) = Tg_{OG}(m,P)Tg_{O_3}(m,U_{O_3})\left[\rho_{atm}(\theta_s,\ \theta_v,\ \phi,\ P,\ Aer,U_{H_2O})+Tr_{atm}(\theta_s,\ \theta_v,\ P,\ Aer)\frac{\rho_s}{1-S_{atm}(P,Aer)\rho_s}Tg_{H_2O}(m,U_{H_2O})\right] \quad (1)$$

where ρ_{TOA} is the top of the atmosphere reflectance; Tg is the gaseous transmission due to other gases (Tg_{OG}), ozone (Tg_{O_3}), and water vapor (Tg_{H_2O}); ρ_{atm} is the atmosphere's intrinsic reflectance; Tr_{atm} is the total atmosphere transmission (both downward and upward); S_{atm} is the atmospheric spherical albedo; and ρ_S is the surface reflectance to be retrieved by the LaSRC.

Similarly, the atmospheric parameters are represented by P (surface pressure), τ_A, ω_0, and P_A (aerosol optical thickness, aerosol single scattering albedo, and aerosol phase function, respectively), U_{H_2O} (integrated water vapor content), and U_{O_3} (integrated ozone content).

The geometrical parameters are given by θ_s (solar zenith angle), θ_v (view zenith angle), and ϕ (relative azimuth angle). The air mass, m, is calculated as the sum of the inverses of the cosine of the solar zenith angle and the view zenith angle.

Water vapor affects the atmospheric intrinsic reflectance, which can be approximated using Equation (2) as described in Ref. [9].

$$\rho_{atm}(\theta_s,\ \theta_v,\ \phi,\ P,\ Aer,U_{H_2O}) = \rho_R(\theta_s,\ \theta_v,\ \phi,\ P)+[\rho_{R+Aer}(\theta_s,\ \theta_v,\ \phi,\ P,\ Aer)-\rho_R(\theta_s,\ \theta_v,\ \phi,\ P)]Tg_{H_2O}\left(m,\ \frac{U_{H_2O}}{2}\right) \quad (2)$$

where ρ_R is the Rayleigh (molecular) scattering reflectance, ρ_{R+Aer} represents the reflectance due to the mixture of molecules and aerosol particles, and $Tg_{H_2O}\left(m,\ \frac{U_{H_2O}}{2}\right)$ represents the gaseous transmission of half the column of atmospheric water vapor. Equation (2) accounts for the mixing and coupling effects of atmospheric gas absorption and scattering by molecules and aerosols.

By combining Equations (1) and (2), the surface reflectance can be inverted using Equation (3).

$$\rho_s = \frac{\frac{\rho_{TOA}}{Tg_{OG}Tg_{O_3}}-(\rho_{R+Aer}-\rho_R)Tg_{H_2O}(m,\ \frac{U_{H_2O}}{2})-\rho_R}{Tr_{atm}Tg_{H_2O}(m,U_{H_2O})\left[1+S_{atm}\frac{\frac{\rho_{TOA}}{Tg_{OG}Tg_{O_3}}-(\rho_{R+Aer}-\rho_R)Tg_{H_2O}\left(m,\ \frac{U_{H_2O}}{2}\right)-\rho_R}{Tr_{atm}Tg_{H_2O}\left(m,U_{H_2O}\right)}\right]} \quad (3)$$

While the atmospheric correction equation (Equation (3)) is relatively straightforward, the primary challenge lies in accurately estimating the atmospheric parameters—water vapor content, ozone content, aerosol properties (aerosol optical thickness, aerosol single scattering albedo, and aerosol phase function), and surface pressure.

In LaSRC, from February 2013 to 30 September 2023, water vapor and ozone content were extracted from the MODIS Fused C2 [51]. This dataset was obtained using four MODIS data sources—MODIS Aerosol Optical Thickness Daily Climate Modeling Grid (MOD09CMA and MYD09CMA) and MODIS SR Daily Climate Modeling Grid (MOD09CMG and MYD09CMG). From 1 October 2023 onward, the water vapor and ozone content are extracted from the Visible Infrared Imaging Radiometer Suite (VIIRS) aerosol daily Level-3 Climate Modeling Grid (CMG) [52].

The inversion of AOD is based on the MODIS Collection 6 surface reflectance algorithm, which evolves from the Collection 5 algorithm and originates from the work of Kaufman et al. [53]. The relationship between the blue and red bands is utilized to retrieve AOD, with a detailed explanation provided by Vermote et al. in their work [9].

The surface pressure is calculated using the elevation data derived from the Earth Topography Five Minute Grid (ETOPO5) (CMGDEM), which can be found at [49]. Using

the elevation data, z (m), the surface pressure, P, is calculated by setting the sea level pressure to 1013 hectopascals (hPa) using Equation (4).

$$P = 1013e^{-z/8500} \quad (4)$$

Equation (4) demonstrates that the surface pressure at a given location is independent of environmental conditions, as it is solely determined by elevation. From Equations (1)–(3), it can be seen that the surface pressure is used in the calculation of the intrinsic reflectance of the atmosphere (ρ_{atm}), Rayleigh scattering reflectance (ρ_R), reflectance due to the mixture of molecules and aerosol particles (ρ_{R+Aer}), total atmospheric transmission (upward and downward) (Tr_{atm}), atmospheric spherical albedo (S_{atm}), and gaseous transmission of other gases (Tg_{OG}). Thus, it is imperative to accurately estimate the surface pressure for the accurate estimation of surface reflectance. However, in LaSRC, the scene center surface pressure, calculated using the described methodology, is applied uniformly to all pixels during the correction process. This approach introduces discrepancies in surface reflectance, particularly for pixels with elevations differing from that of the scene center.

3.1.2. Calculation of LaSRC Surface Pressure for Landsat 8 Scene

The procedure used in the calculation of the LaSRC surface pressure for a Landsat 8 scene is shown in Figure 6.

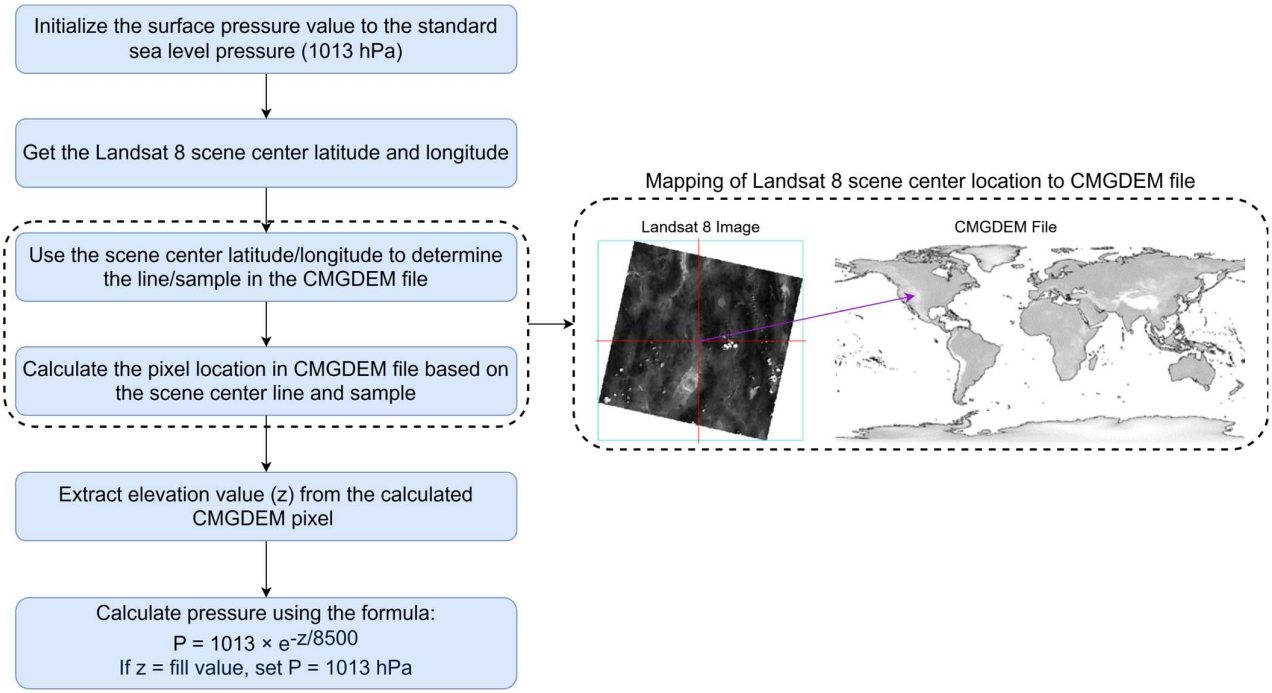


Figure 6. Flow chart for the calculation of scene center surface pressure in LaSRC.

Initially, the surface pressure value was set to the standard sea level pressure (1013 hPa). The scene center latitude and longitude of the Landsat 8 image were then extracted. In LaSRC, the process for determining the scene center is not clearly defined, and the scene center information is not included in the Landsat 8 metadata file. Therefore, in this study, the scene center latitude and longitude were estimated by averaging the coordinates of the four corners of the Landsat 8 image. Using these coordinates, the corresponding line and sample were identified within the CMGDEM file. Subsequently, the pixel location in the CMGDEM file was calculated based on the scene center line and sample. The elevation data (z) was extracted from the determined CMGDEM pixel. Finally, the surface pressure was

computed using Equation (4). If the elevation value was unavailable (fill value), the surface pressure was set to 1013 hPa, maintaining consistency in the absence of valid elevation data.

3.2. Data Processing for RadCalNet Sites

The processing of the RadCalNet data (Figure 7) began with the identification of the coincident dates of RadCalNet measurement and Landsat 8 passage date. Once the coincident dates were identified, additional filtering was applied. This filter was developed after rigorous testing on various test cases using RVUS datasets collected on days with complete RadCalNet measurements (13 in total), recorded at 30-min intervals throughout the day. These tests aimed to establish robust criteria to ensure the highest quality data for further analysis. Notably, the Landsat 8 overpass time for RVUS typically falls between 18:00 and 18:30 UTC, a window that played a key role in shaping the filtering strategy. The details of this process are outlined in the following paragraph.

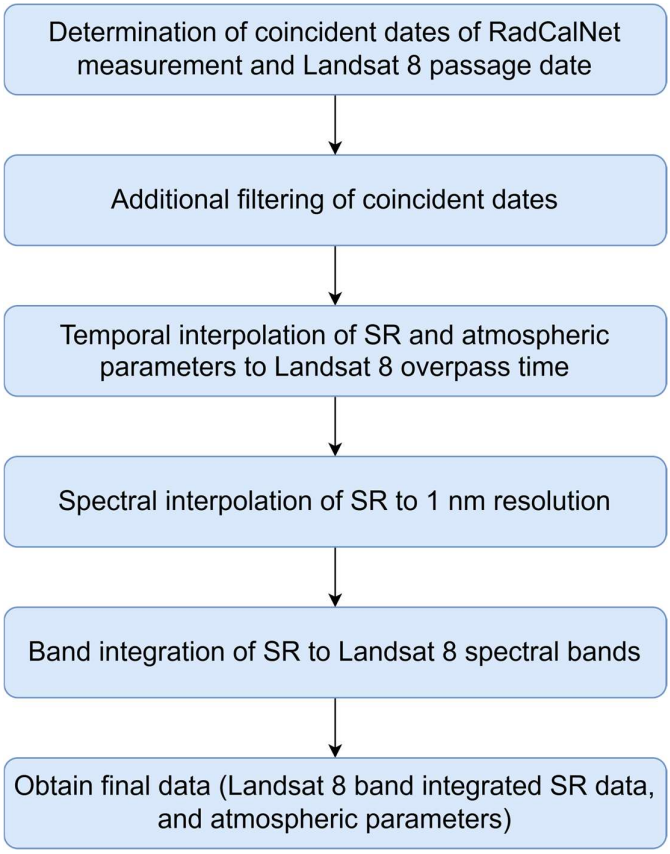


Figure 7. Flow chart of RadCalNet data processing.

Initially, the following three filtering criteria were selected for RadCalNet measurements:

1. There must be at least one RadCalNet measurement within one hour before the satellite overpass.
2. There must be at least one RadCalNet measurement within one hour after the satellite overpass.
3. A minimum of four RadCalNet measurements out of 13 available measurements throughout the day (from 17:00 to 23:00 UTC) must be present.

To test these criteria, the following fourteen distinct test cases were designed:

- Test case 1—All 13 RadCalNet measurements were included.
- Test case 2—The RadCalNet measurement at 18:30 was removed.

- Test case 3—Criterion 1 was removed (RadCalNet measurements at 17:30 and 18:00 were excluded).
- Test case 4—Criterion 2 was removed (RadCalNet measurements at 19:00 and 19:30 were excluded).
- Test case 5—Both Criteria 1 and 2 were removed (RadCalNet measurements from 17:30 to 19:00 were excluded).
- Test case 6—Criteria 1 and 2 were retained, but Criterion 3 was removed, leaving only three RadCalNet measurements.
- Test cases 7 to 14—Criteria 1, 2, and 3 were retained, and the number of RadCalNet measurements varied between 4 and 11, incrementing by one RadCalNet measurement for each test case.

These fourteen test cases were created to systematically assess the impact of both the number of RadCalNet measurements and the presence of each filtering criterion. By designing test cases that individually remove specific criteria (as in test cases 3–6) and others that incrementally vary the number of measurements (test cases 1–2, 7–14), the approach enabled a comprehensive sensitivity analysis of the filters. This design allowed for the evaluation of both isolated and combined effects of the filtering criteria on test case performance, ensuring that the methodology is robust under different scenarios of RadCalNet measurements.

Each test case produced a unique combination of measurements, resulting in different logical masks specifying which data points were included. The number of logical masks varied across test cases, generating hundreds of configurations for some test cases, which ensured a thorough assessment of all possible measurement combinations.

For each of the test cases, the reflectance value closest to the Landsat 8 overpass time (18:30 UTC) was predicted. The test cases were then evaluated based on Root Mean Squared Error (RMSE) across the wavelengths corresponding to Landsat 8's Relative Spectral Response (RSR). The test case that required the fewest RadCalNet measurements while maintaining the RMSE within the uncertainty range of RVUS surface reflectance (below one reflectance unit) was selected as the additional filter.

Additionally, dates falling outside the 1σ temporal standard deviation were visually inspected alongside the RadCalNet input file. These dates were excluded if anomalous conditions, such as cloud cover over the ROI, wet surfaces, or vegetation on the surface, were identified.

Subsequently, the RadCalNet surface reflectance was temporally interpolated to match Landsat 8 overpass time using quadratic interpolation. Quadratic interpolation was selected because surface reflectance is typically observed to increase until solar noon and then decrease in a quadratic pattern. In contrast, linear interpolation was applied to atmospheric parameters (ozone, water vapor, temperature, surface pressure, AOD, and aerosol angstrom coefficient) since these parameters vary in a stochastic manner over short periods and do not follow a predictable trend.

After this, a thorough evaluation was conducted to assess the necessity of spectral interpolation. For this analysis, 1-nanometer (nm) hyperspectral surface reflectance data from RVUS was utilized. The 1 nm data were band-integrated to Landsat 8 RSR, and this was regarded as the ground truth. Subsequently, the original 1 nm hyperspectral data were band-averaged to a 10 nm resolution, matching the 10 nm interval of RadCalNet measurements. This served as the test dataset for the analysis. The band-averaged data were first directly band-integrated to Landsat 8 bands. Additionally, the band-averaged data were interpolated using four methods—linear, spline, makima, and Piecewise Cubic Hermite Interpolating Polynomial (PCHIP)—and each interpolated dataset was band-integrated to Landsat 8 bands. The reflectance differences between the ground truth and

the outputs from these five methods were then compared, and the interpolation method with the smallest reflectance difference across the Landsat 8 bands was selected.

Finally, the spectrally interpolated reflectance data were band-integrated to Landsat 8 using Equation (5).

$$\rho_{L8\ band,RadCalNet} = \frac{\sum_{\lambda_2}^{\lambda_1} \rho_{\lambda}^{H} \times RSR_{\lambda}}{\sum_{\lambda_2}^{\lambda_1} RSR_{\lambda}} \quad (5)$$

where $\rho_{L8\ band,RadCalNet}$ represents the integrated equivalent reflectance of RadCalNet predicted SR in the Landsat 8 sensor band; λ_1 and λ_2 define the wavelength range of the band of interest at 1 nm intervals; RSR_{λ} is the relative spectral response of Landsat 8; and ρ_{λ}^{H} denotes the spectrally interpolated surface reflectance from RadCalNet.

3.3. Data Processing for Arable Mark 2 Sites

Four major steps were followed for the comparison of the Arable Mark 2 SR measurements with the Landsat 8 SR. Firstly, the SR data from the Arable Mark 2 were cross-calibrated against an Analytical Spectral Devices (ASD) spectroradiometer to ensure measurement consistency and reliability. Since the direct validation of Arable SR with the Landsat 8 SR was not possible due to the difference in spectral bands, the second step involved deriving hyperspectral surface reflectance using the SDSU in situ hyperspectral vegetative library, which spans over two decades. In the third step, coincident dates between the Arable Mark 2 measurements and Landsat 8 overpass dates were identified. Finally, the derived hyperspectral SR was spectrally integrated to match Landsat 8 bands to obtain the reflectance value for each Landsat 8 band. Detailed processing steps for the Arable Mark 2 data are available in the work by Pathiranage et al. [43].

Surface pressure data for Arable sites in Brookings and Arlington were obtained from the National Centers for Environmental Information (NCEI) database. Specifically, this study utilized the Global Historical Climatology Network-Hourly (GHCNh), Version 1 dataset [54]. GHCNh is a comprehensive, well-documented collection, along with quality control checks of meteorological observations from fixed weather stations worldwide, spanning from the late 18th century to the present. It integrates approximately 110 data sources and is updated daily using data streams from the United States Air Force and National Oceanic and Atmospheric Administration (NOAA) Surface Weather Observations data streams. In this study, hourly station-level pressure data from GHCNh were used, and values were linearly interpolated to match with Landsat 8 overpass times. While the pressure data for Brookings are available in the NCEI database (with station ID USW00094902 and station name Brookings), the data are not available for Arlington. Hence, Equation (6) was used to spatially interpolate the pressure data at Arlington from Brookings station.

$$P = P_0 \times \left(1 - \frac{L \times (h - h_0)}{T_o + 273.15}\right)^{\frac{gM}{RL}}, \quad (6)$$

where P is the pressure at Arlington at height h (in meters); P_0 is the reference pressure of Brookings at height h_0; L is the temperature lapse rate (0.0065 K/m); T_0 is the reference temperature at Brookings in °C; M is the molar mass of Earth's air (0.0289644 kg/mol); g is the gravitational acceleration (9.80665 m/s^2); and R is the universal gas constant (8.3144598 J/(mol·K).

Finally, the spatially interpolated pressure of Arlington was linearly interpolated to Landsat 8 passage time to obtain the pressure at the time of satellite overpass.

3.4. Landsat 8 Surface Reflectance Calculation

The DN (digital number) values from the Landsat 8 image were converted to surface reflectance using the radiometric coefficients in the Landsat 8 metadata file, following Equation (7) provided by the USGS [55].

$$\rho_{band,Landsat} = M_{band} \times DN + A_{band}, \quad (7)$$

where $\rho_{band,Landsat}$ is the surface reflectance value of each pixel of the Landsat 8 band, M_{band} is the band-specific multiplicative scale factor, and A_{band} is the band-specific additive scale factor.

During this process, the Quality Assessment (QA) band bits were used to mask pixels affected by cloud, cloud shadow, or snow. These masked pixels were excluded from the surface reflectance calculation to ensure that only high-quality pixels were used. The reflectance values of unmasked pixels within the region of interest (ROI) were then averaged to obtain the final surface reflectance value.

3.5. Comparison of Surface Reflectance Difference with Surface Pressure Ratio

After dataset preparation, the Landsat 8 data were compared with the ground truth RadCalNet and Arable data to analyze the discrepancies. A comparative analysis was then conducted to assess the relationship between surface reflectance differences and the surface pressure ratio. The surface reflectance difference was determined by subtracting the Landsat 8 reflectance from the corresponding ground truth surface reflectance (RadCalNet or Arable). Concurrently, the surface pressure ratio was obtained by dividing the surface pressure obtained via LaSRC by the ground-based pressure measurements. This evaluation provided insights into the consistency and potential biases in Landsat 8 surface reflectance retrievals under varying pressure ratios.

3.6. Selection of Fit

Pressure influences a number of parameters of Equation (3): intrinsic reflectance of the atmosphere (ρ_{atm}) given by $((\rho_{R+Aer} - \rho_R)Tg_{H_2O}\left(m, \frac{U_{H_2O}}{2}\right) + \rho_R)$, Rayleigh scattering reflectance (ρ_R), reflectance due to the mixture of molecules and aerosol particles (ρ_{R+Aer}), gaseous transmission of other gases (Tg_{OG}), total atmospheric transmission (Tr_{atm}), and atmospheric spherical albedo (S_{atm}). Thus, there is no easy fix to the problem induced by the discrepancy of surface pressure.

Hence, to derive the problem fix, the primary objective was set to determine the equation that better characterizes the relationship between the surface reflectance differences across varying surface pressure ratios and aligns with the complexity of the LaSRC equation. In theory, the ideal model should yield residuals with a mean near zero (indicating minimal bias), a small standard deviation (reflecting tight variability), and no discernible patterns (indicating the absence of systematic over- or underestimation). Additionally, the residuals should exhibit randomness, as verified using the Wald–Wolfowitz runs test. Meeting these criteria ensures that the model minimizes systematic errors and enhances its applicability for atmospheric correction. In case of similar performance, priority was given to the model that could, to some extent, justify the mathematical complexity of the LaSRC Equation (3).

To satisfy these criteria, seven weighted regression models were evaluated: linear, quadratic, cubic, fourth-order polynomial, logarithmic, and two exponential forms (a double exponential and an exponential with a constant term). Weighting was applied as (1/truth uncertainty percentage), thereby placing greater emphasis on measurements with lower uncertainty.

3.7. Validation

For the model generation, data up to 2023 was used. Hence, for validation purposes, RadCalNet data from 2024 was used. Only the 2024 RadCalNet data were used for validation because they included the sites that were most impacted by pressure-related discrepancies in the LaSRC. The 2024 RadCalNet data, being the most recent dataset, ensured that the validation reflected the current conditions and provided a robust test of the model's performance. The methodology for processing the RadCalNet and Landsat 8 data required for validation was the same as described in Sections 3.2 and 3.4. The performance of the model on the validation dataset was evaluated through three key metrics: root mean square deviation (RMSD), mean error (ME), and mean absolute error (MAE), which are the commonly used evaluation metrics for satellite reflectance products [11].

3.7.1. Root Mean Square Deviation

RMSD quantifies the magnitude of the deviation between the Landsat 8 image-derived reflectance ($\hat{r}(\lambda)$) and ground-truth reflectance ($r(\lambda)$) corresponding to each band (λ). In this work, the RMSD was calculated using Equation (8), where N is the number of observations.

$$RMSD = \sqrt{\frac{1}{N}\sum_{i=1}^{N}(r_i(\lambda) - \hat{r}_i(\lambda))^2} \quad (8)$$

3.7.2. Mean Error

ME is the average difference between the ground truth surface reflectance and Landsat 8 surface reflectance. In this study, ME was computed using Equation (9).

$$ME = \frac{1}{N}\sum_{i=1}^{N}(r_i(\lambda) - \hat{r}_i(\lambda)) \quad (9)$$

3.7.3. Mean Absolute Error

MAE gives the average absolute magnitude of the difference between the ground truth surface reflectance and Landsat 8 surface reflectance. In this study, MAE was calculated using Equation (10).

$$MAE = \frac{1}{N}\sum_{i=1}^{N}|r_i(\lambda) - \hat{r}_i(\lambda)| \quad (10)$$

4. Results

4.1. Land Surface Reflectance Code

4.1.1. Surface Reflectance Inversion

Figure 8 shows an example of surface reflectance inversion through LaSRC. The Level 1 RGB composite image is shown in Figure 8a, and the Level 2 RGB composite image is shown in Figure 8b. The Level 2 image has been corrected for atmospheric effects through LaSRC.

4.1.2. Calculation of LaSRC Surface Pressure for Landsat 8 Scene

Figure 9 shows the LaSRC-calculated elevation and surface pressure for the Landsat 8 scenes over different sites used in this study. The elevation and surface pressure used for atmospheric correction of all the Landsat 8 scenes were consistent throughout the time series graph. Most sites have elevation and surface pressure fluctuating between two values. The surface pressure of the LCFR site was constant (1013 hPa) throughout the time series, as the elevation is always the fill value. Similarly, BSCN has different scene center elevations and surface pressures for different paths and rows.

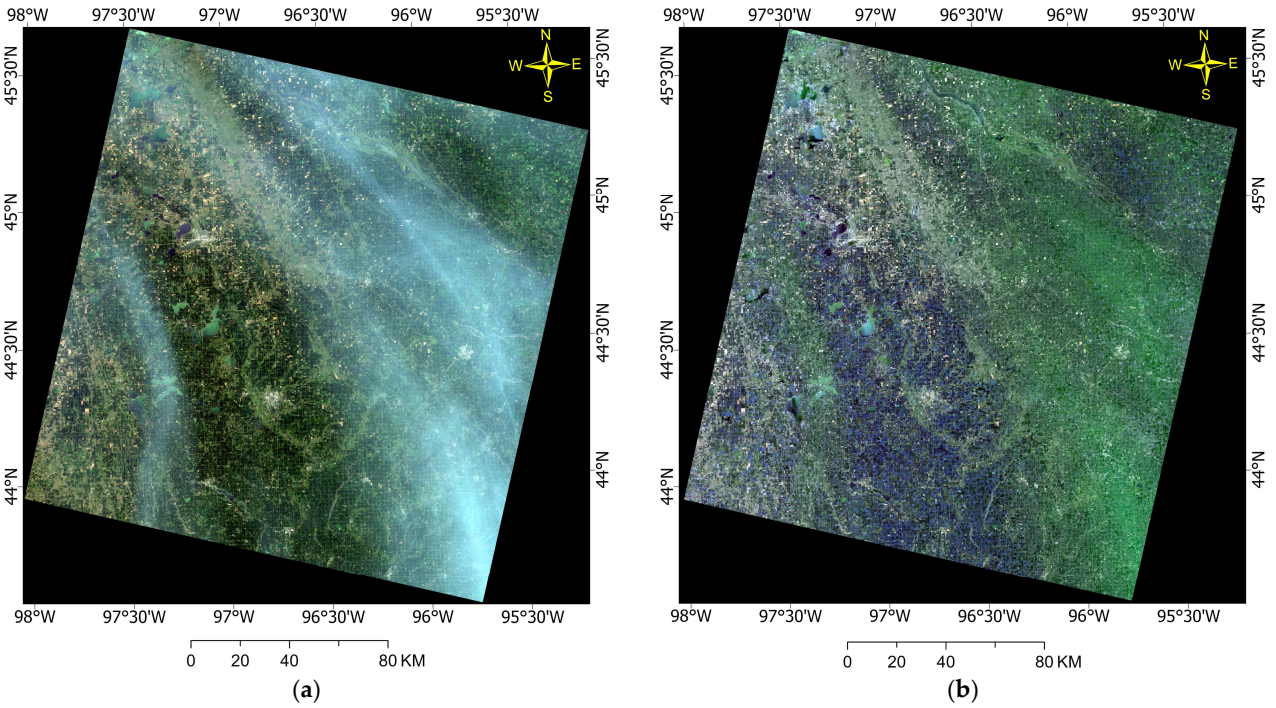


Figure 8. Image acquired by Landsat 8 OLI over Brookings, South Dakota, on 11 August 2018. (**a**) Level 1 image. (**b**) Level 2 image generated by LaSRC.

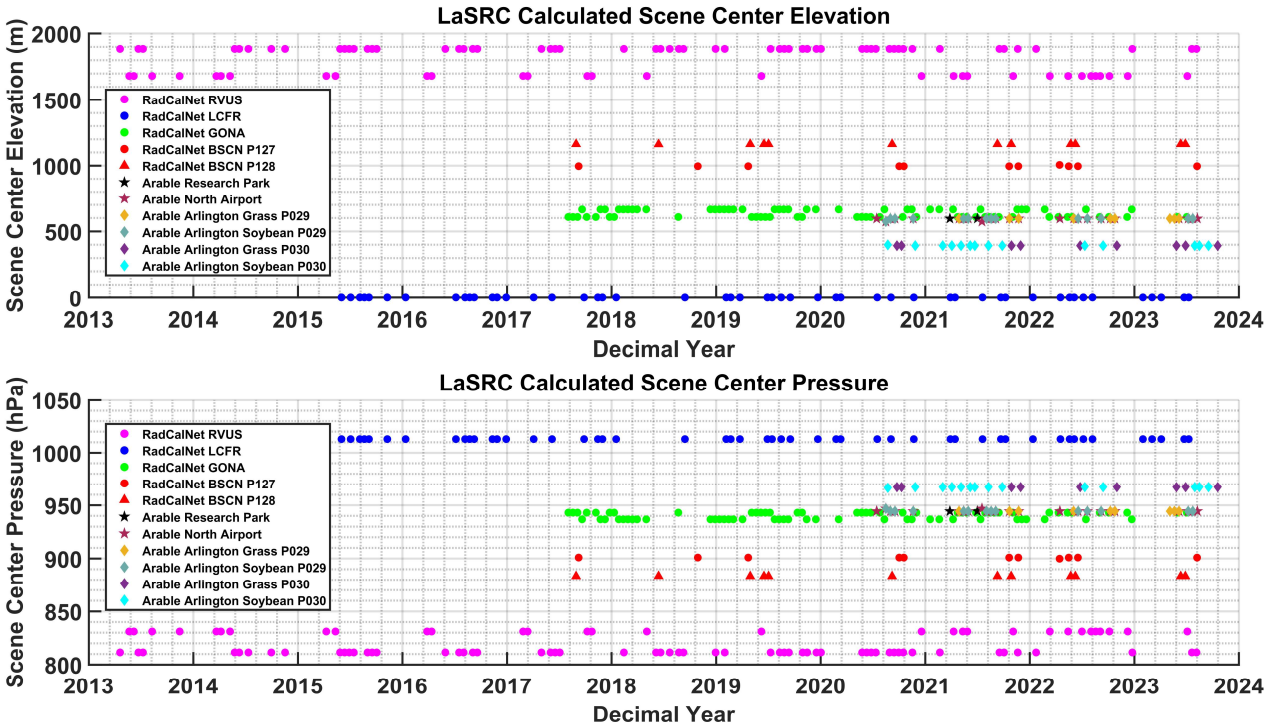


Figure 9. Scene center elevation and surface pressure calculated from LaSRC over the RadCalNet and Arable Mark 2 sensor sites for Landsat 8 scenes.

Figure 10 illustrates the process using sample Landsat 8 scenes and the ROI of each site. There is a difference in the scene center elevation calculated by LaSRC and the actual elevation for each site. Among them, Railroad Valley Playa has the highest difference in elevation. Since the LaSRC-calculated scene center surface pressure is dependent on the elevation (Equation (4)), with the elevation difference, it is clear that there will be a difference in the surface pressure at the ground truth.

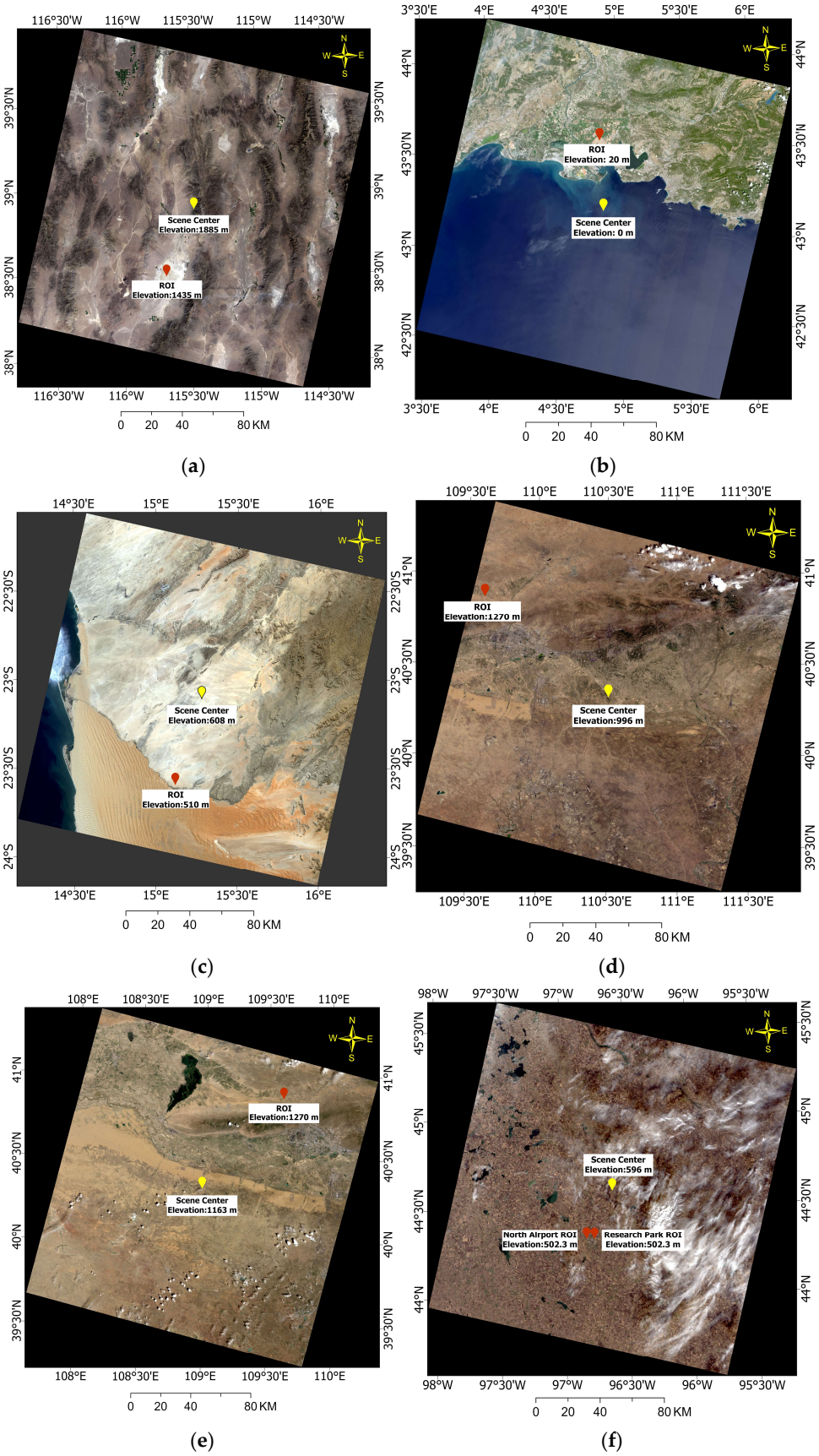


Figure 10. *Cont.*

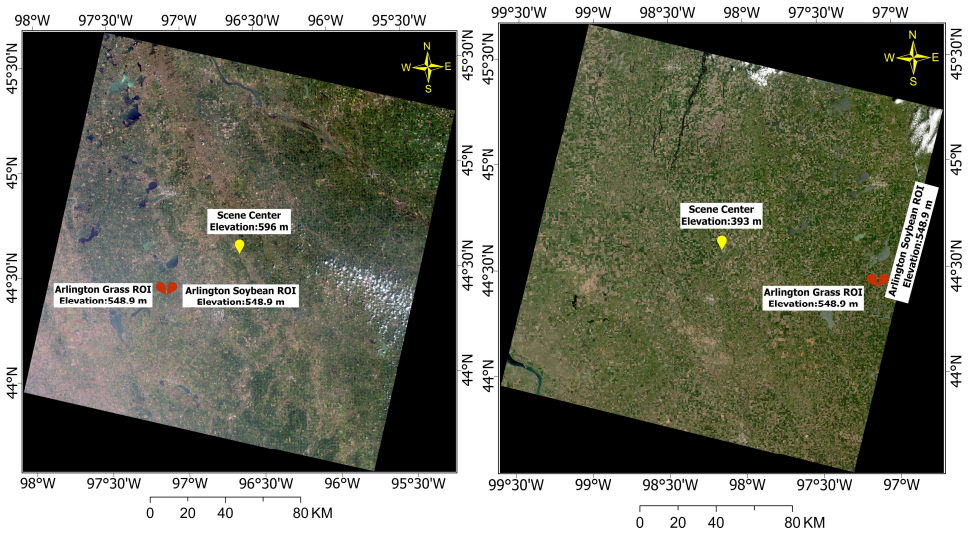


Figure 10. Landsat 8 TOA RGB composite images showing the scene centers, ROI, and their elevation for the sites used in this study. The yellow pin represents the scene center location of each Landsat 8 image, and the red pin represents the center coordinates of the ROI of the sites. (**a**) RVUS; (**b**) LCFR; (**c**) GONA; (**d**) BSCN WRS-2 Path 127 Row 32; (**e**) BSCN WRS-2 Path 127 Row 32; (**f**) Research Park and North Airport; (**g**) Arable Arlington WRS-2 Path 029 Row 029; and (**h**) Arable Arlington WRS-2 Path 030 Row 029.

The detailed statistics of the sample images used in Figure 10 are presented in Table 2. It shows that RVUS, followed by BSCN Path 127, had the highest pressure difference between the actual surface pressure at the site and the LaSRC-calculated scene center surface pressure. It was because the RVUS had the scene center at the top of the hill (see Figure 10a) with an elevation of 1885 m, whereas the actual site elevation was 1435 m, leading to an elevation difference of 450 m. Furthermore, the surface pressure at the scene center was not a real pressure measured at the particular location; it is the elevation-based pressure estimated by Equation (4). The same conclusion could be drawn from the BSCN Path 127. From Table 2 and Figure 10d,e, the difference in elevation between BSCN Path 127 and BSCN Path 128 could be seen. The elevation difference between the site and scene center at BSCN Path 127 was greater than that of BSCN Path 128. This caused the pressure difference at BSCN Path 127 to be greater than that of BSCN Path 128.

4.2. Data Processing for RadCalNet Sites

Figure 11 shows the RMSE of each of the fourteen test cases (as described in Section 3.2) evaluated for the determination of the additional filter. Test case 5 had the highest RMSE since the nearest RadCalNet measurements to the test instance (18:30 UTC) were missing for this test case. Moreover, test case 1, which included all thirteen RadCalNet measurements, had the lowest RMSE. Test case 7, which represented the initial filtering criteria of having at least one RadCalNet measurement both before and after one hour of satellite overpass and a minimum of four valid RadCalNet measurements throughout the day, was selected because its RMSE value of 0.0091 was less than one unit of reflectance and fell within the uncertainty range of the RadCalNet RVUS surface reflectance. This test case also provided a balance between data availability and data quality.

Table 2. Difference in LaSRC-calculated surface pressure and actual surface pressure for the selected Landsat 8 passage dates of the sites used in this study.

Site	Date	LaSRC Elevation (m)/ Pressure (hPa)	Actual Elevation (m)/ Pressure (hPa)	Difference of Actual Pressure and LaSRC Pressure (hPa)
RVUS	27 August 2019	1885/811.52	1435/859.00	47.48
LCFR	16 August 2019	0/1013.00	20/1014.92	1.92
GONA	27 June 2021	608/943.07	510/955.01	11.94
BSCN Path 127	18 June 2022	996/900.99	1270/862.00	−38.99
BSCN Path 128	17 June 2022	1163/883.46	1270/864.00	−19.46
Arable Research Park	23 November 2021	596/944.40	502.3/946.38	1.98
Arable North Airport	23 November 2021	596/944.40	502.3/946.38	1.98
Arable Arlington Grass Path 029	7 September 2022	596/944.40	548.9/957.19	12.79
Arable Arlington Soybean Path 029	7 September 2022	596/944.40	548.9/957.19	12.79
Arable Arlington Grass Path 030	12 July 2022	393/967.23	548.9/953.72	−13.51
Arable Arlington Soybean Path 030	12 July 2022	393/967.23	548.9/953.72	−13.51

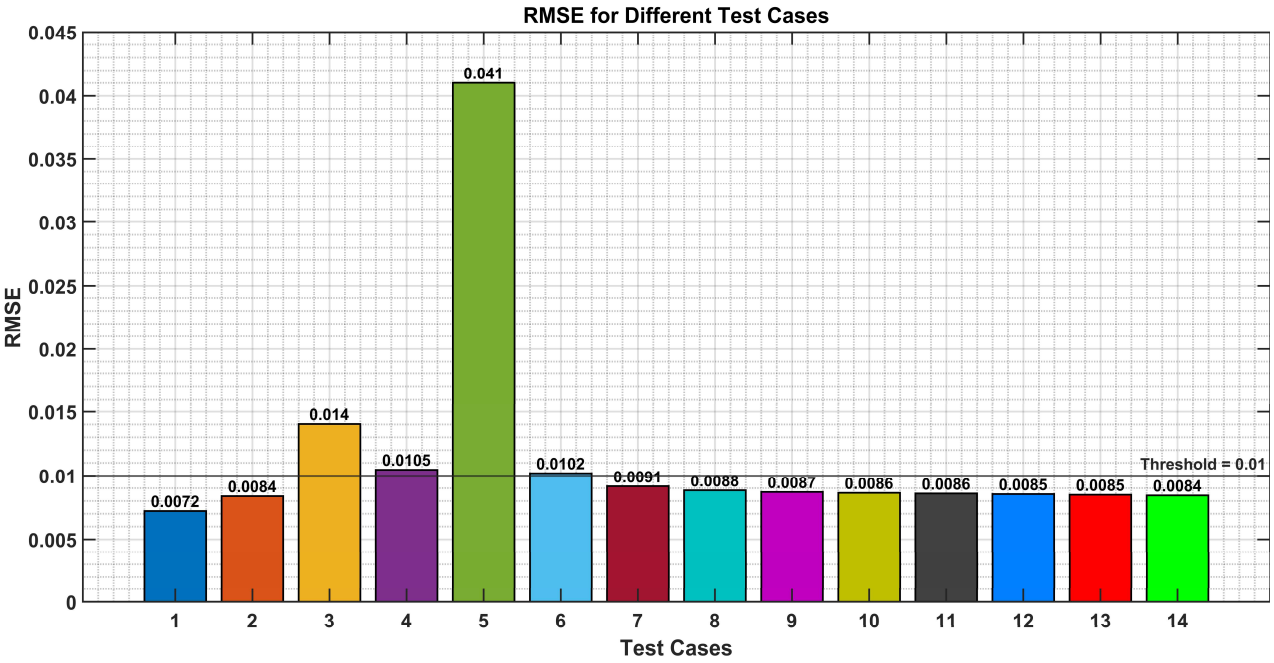


Figure 11. Bar graph showing RMSE for 14 different test cases used to determine the filtering for selecting the RadCalNet data. The RMSE is in the reflectance unit.

Similarly, Figure 12 shows the comparison of the five methods of interpolation used to assess the necessity of spectral interpolation. As visible in the chart, the band averaged 10 nm (similar to 10 nm measurements provided by RadCalNet) and had the highest difference across all the bands, except for the SWIR bands. This justified the use of the interpolation of RadCalNet data to 1 nm rather than using the raw 10 nm data provided by RadCalNet.

The detailed statistics of the difference between the Landsat 8 band-integrated truth reflectance and interpolated reflectance for different interpolation methods can be found in Table A1. Among them, the spline interpolation method was selected since it had the

smallest difference with ground truth across all the Landsat 8 SR bands except for the green and SWIR 2 bands.

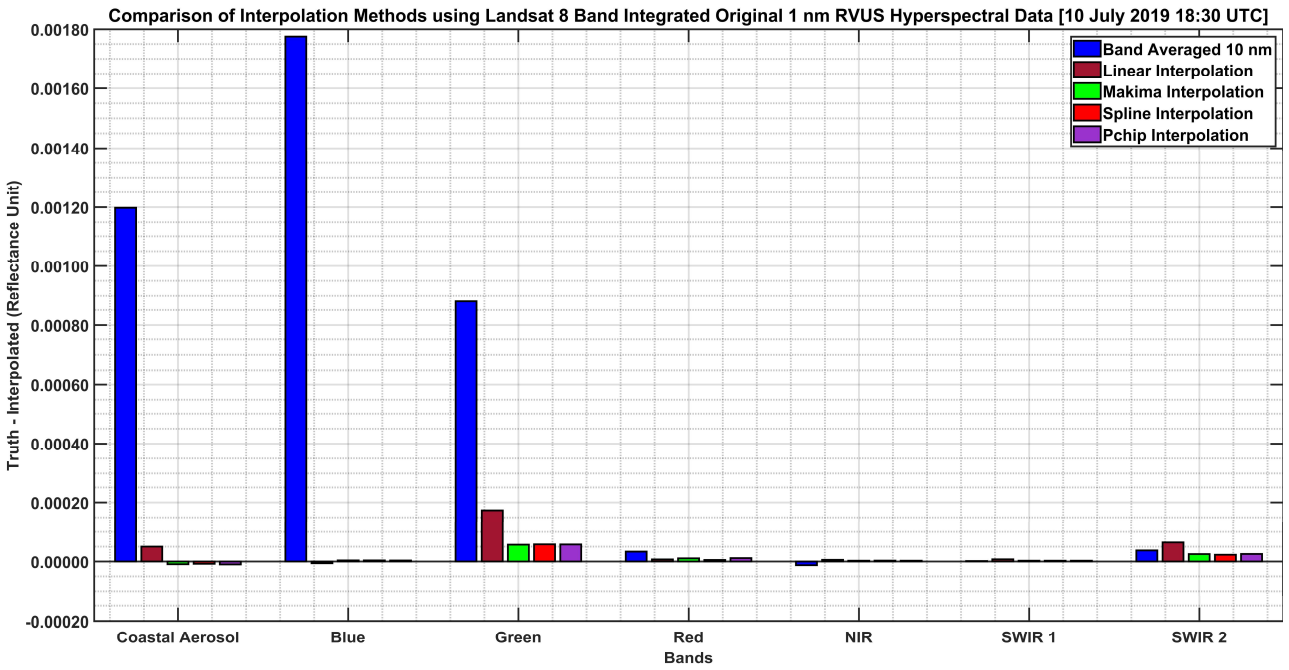
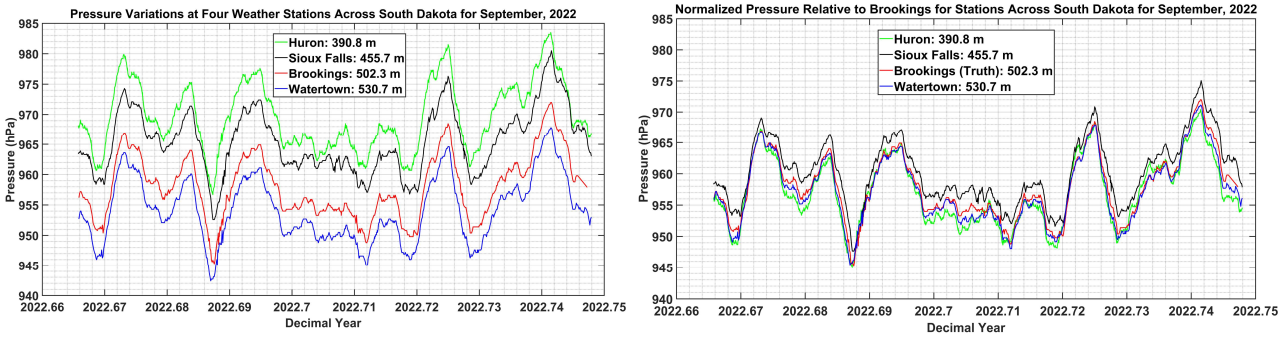


Figure 12. Comparison of five methods of band integration (band averaged 10 nm, linear, makima, spline, and PCHIP interpolation) to Landsat 8 using RVUS 1 m hyperspectral surface reflectance data.

4.3. Data Processing for Arable Mark 2 Sites

The detailed results of SR processing of Arable sites located in Brookings and Arlington can be found in the work by Pathiranage et al. [43]. The atmospheric data (surface pressure) for the sites located at Brookings was sourced from the NCEI. Since the surface pressure at Arlington was not available at NCEI, the pressure variations across different stations nearer to Arlington were first analyzed. This was primarily performed in order to assess if the pressure data of Brookings could be directly used for the Arlington sites. Figure 13a shows the pressure at four different stations near Arlington, SD, for the month of September 2022, where a considerable difference between the pressures at different locations as per elevation can be observed. Huron, having the lowest elevation, had the highest pressure, followed by Sioux Falls, Brookings, and Watertown. It should be noted that the real pressure measured at each station fluctuates within approximately 25 hPa for a single month. Thus, unlike the pressure used in LaSRC, which is a static value based on the scene center elevation, the pressure at the particular location/elevation can change based on the surrounding environmental conditions.

Since there were considerable differences between the pressure at different locations across South Dakota, Equation (6) was used to normalize the pressure at three different stations, i.e., Huron, Sioux Falls, and Watertown, and its accuracy with the real pressure measured at Brookings was analyzed. As can be seen in Figure 13b, the normalized pressure from three stations differed from the real pressure at Brookings by less than five hPa (approximately less than 0.53% error). This illustrates that the pressure data for a particular location can be interpolated with minimal error from the measured pressure at a nearby weather station. Therefore, pressure data from Brookings, the nearest weather station to Arlington, was used to spatially interpolate the pressure data for Arlington.



(**a**) (**b**)

Figure 13. (**a**) Pressure variations at weather stations located at Huron, Sioux Falls, Brookings, and Watertown for September 2022. (**b**) Normalized pressure relative to Brookings for Huron, Sioux Falls, and Watertown for September 2022.

4.4. Comparison of Landsat 8 Surface Reflectance with Ground Truth Surface Reflectance

A comparison was made between the surface reflectance of the Landsat 8 image and the ground truth measurements. As shown in Figure 14, discrepancies were clearly seen in coastal aerosol and blue bands since the regression line was farther from the 1-to-1 line. A slight discrepancy was noticeable in the green band, too, but that will be verified later through statistical tests. Overall, the discrepancies could be observed in the shorter bands and were fading away as we moved towards longer bands.

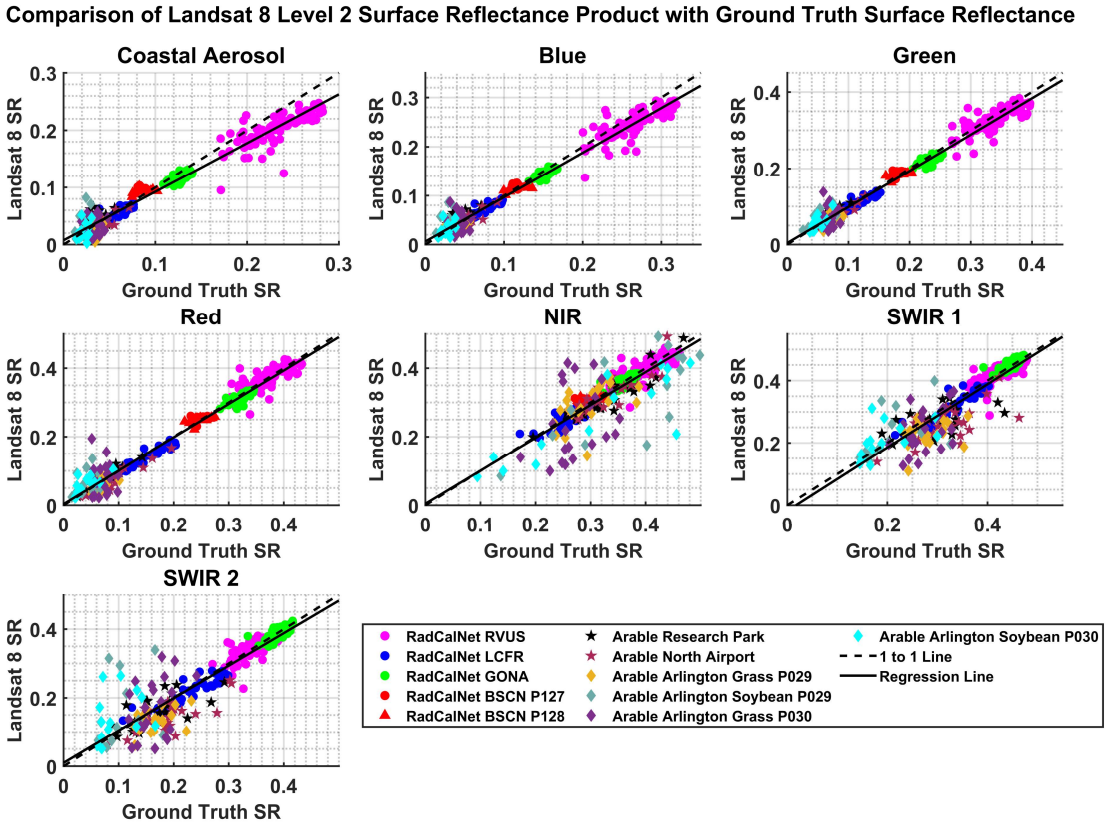


Figure 14. Comparison of the Landsat 8 Level 2 surface reflectance product with the ground truth surface reflectance measurements from RadCalNet and Arable Mark 2 sensors.

4.5. Comparison of Surface Reflectance Difference with Surface Pressure Ratio

Our findings indicate that the discrepancy observed in Figure 14 was due to the inaccurate estimation of surface pressure for the RadCalNet and Arable sites. LaSRC uses

a scene center surface pressure calculated as described in Section 3.1.2 to correct for the atmospheric effects for the entire scene pixels, although the actual surface pressure at the ROI of sites may vary from that of the scene center surface pressure.

The impact of surface pressure difference on surface reflectance difference was, at first, assessed for the coastal aerosol band. Figure 15 shows that as the surface pressure ratio increases (hence, the pressure difference), the reflectance difference also increases. RVUS is the most impacted site, followed by BSCN, since they have the higher surface pressure difference due to the higher elevation difference and, hence, the larger surface reflectance difference. The sites that lie in the middle of the plots mostly have flat surfaces, and hence, the elevation and surface pressure difference is smaller for them, subsequently resulting in smaller surface reflectance differences.

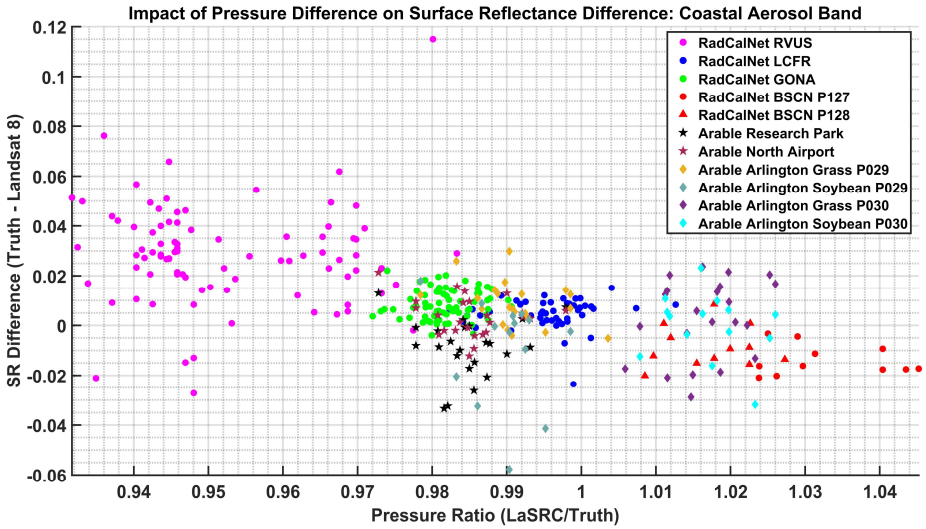


Figure 15. Impact of pressure difference on the surface reflectance difference between the ground truth and the Landsat 8 for the coastal aerosol band.

Table 3 presents the summary of the surface pressure differences' temporal mean, along with the standard deviation and its impact on the surface reflectance difference for each of the sites included in this study. The surface reflectance difference is higher for the sites where there is a substantial pressure difference, such as for RVUS and BSCN.

Table 3. Site-wise surface pressure differences' temporal mean and the corresponding surface reflectance difference mean, along with the standard deviation.

Site	Mean Difference Between Actual Pressure and LaSRC Pressure (hPa)	Mean Difference Between Actual SR and Landsat 8 SR (Reflectance Unit)
RVUS	41.12 ± 11.12	0.0285 ± 0.0202
LCFR	4.55 ± 6.01	0.0048 ± 0.0060
GONA	17.37 ± 3.81	0.0084 ± 0.0059
BSCN Path 127	-28.38 ± 6.93	-0.0140 ± 0.0061
BSCN Path 128	-14.97 ± 5.13	-0.0085 ± 0.0083
Arable Research Park	14.68 ± 5.26	-0.0088 ± 0.0116
Arable North Airport	14.18 ± 5.21	0.0034 ± 0.0079
Arable Arlington Grass Path 029	8.39 ± 5.12	0.0084 ± 0.0088
Arable Arlington Soybean Path 029	9.80 ± 4.86	-0.0092 ± 0.0213
Arable Arlington Grass Path 030	-15.78 ± 4.99	0.0024 ± 0.0160
Arable Arlington Soybean Path 030	-16.19 ± 5.11	-0.0003 ± 0.0134

After the coastal aerosol band, other bands of Landsat 8 were subsequently analyzed. Figure 16 shows the impact of surface pressure difference on surface reflectance difference for six other bands of Landsat 8. The effect of surface pressure difference is visible on the blue and green bands, after which the impact is hardly noticeable on the red, NIR, SWIR 1, and SWIR 2 bands.

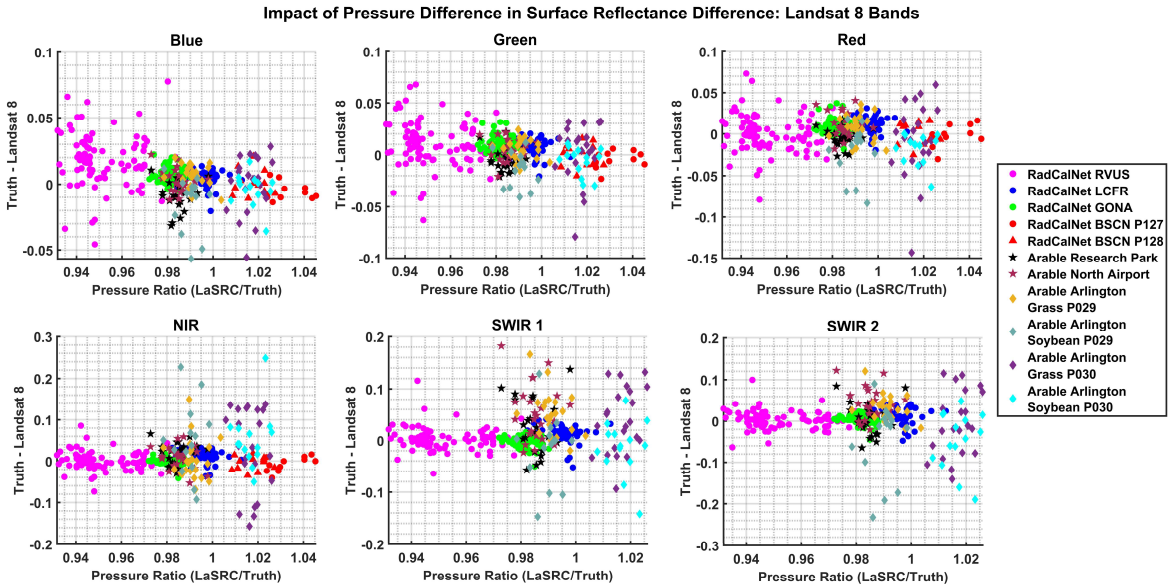


Figure 16. Impact of surface pressure difference on the surface reflectance difference between the ground truth and the Landsat 8 for blue, green, red, NIR, SWIR 1, and SWIR 2 bands.

4.6. Selection of Fit

At first, the effect of pressure-related discrepancy was assessed for the coastal aerosol band. To model the impact on surface reflectance difference in this band, seven different types of weighted fits were analyzed, which are presented in the Appendix A section (Figures A1–A7).

The residual mean error and standard deviation of the seven different weighted fits for the coastal aerosol band are presented in Table 4. Among these fits, linear and logarithmic fits were not selected due to their relatively high mean residuals, high standard deviations, and noticeable pattern of a subtle smiley face in their residual plots. Polynomial 4 fit, despite having the lowest residual metrics, was not selected due to visual signs of overfitting, with concerns about its generalization to data outside the modeled range. Having similar residuals and standard deviation of residuals, exponential fits were chosen over the remaining polynomial fits (quadratic and cubic) for their physical relevance to atmospheric correction. Finally, the exponential fit with a constant term was selected for its comparable performance and simplicity over the complex two exponential terms fit. The selected exponential model with the constant term was statistically significant with the F-statistic of 124 and p-value of 1.79×10^{-41}, which is less than the level of significance, $\alpha = 0.01$ [56].

In addition, the randomness of the residuals of the exponential with the constant model was tested using the Wald–Wolfowitz Runs test. For this, the residuals were sorted according to the increasing order of the surface pressure ratio. The p-value obtained from the Runs test was 0.672, which is greater than the level of significance (0.05), indicating that the residuals followed a random sequence without any underlying pattern.

Subsequently, the exponential with constant model was fitted for the remaining bands of Landsat 8: blue, green, red, NIR, SWIR 1, and SWIR 2, as shown in Figure 17. The statistical results of the fit for all seven bands are presented in Table 5.

Table 4. Comparison statistics for seven different types of fit (linear, quadratic, cubic, polynomial 4, logarithmic, two exponential terms, and exponential with constant) for the coastal aerosol band.

Fit Type	Residual Mean Error (Reflectance Unit)	Residual Standard Deviation (Reflectance Unit)
Linear	−0.0007	0.0150
Quadratic	−0.0005	0.0149
Cubic	−0.0005	0.0149
Polynomial 4	−0.0004	0.0148
Logarithmic	−0.0006	0.0150
Two Exponential Terms	−0.0005	0.0149
Exponential with Constant	−0.0005	0.0149

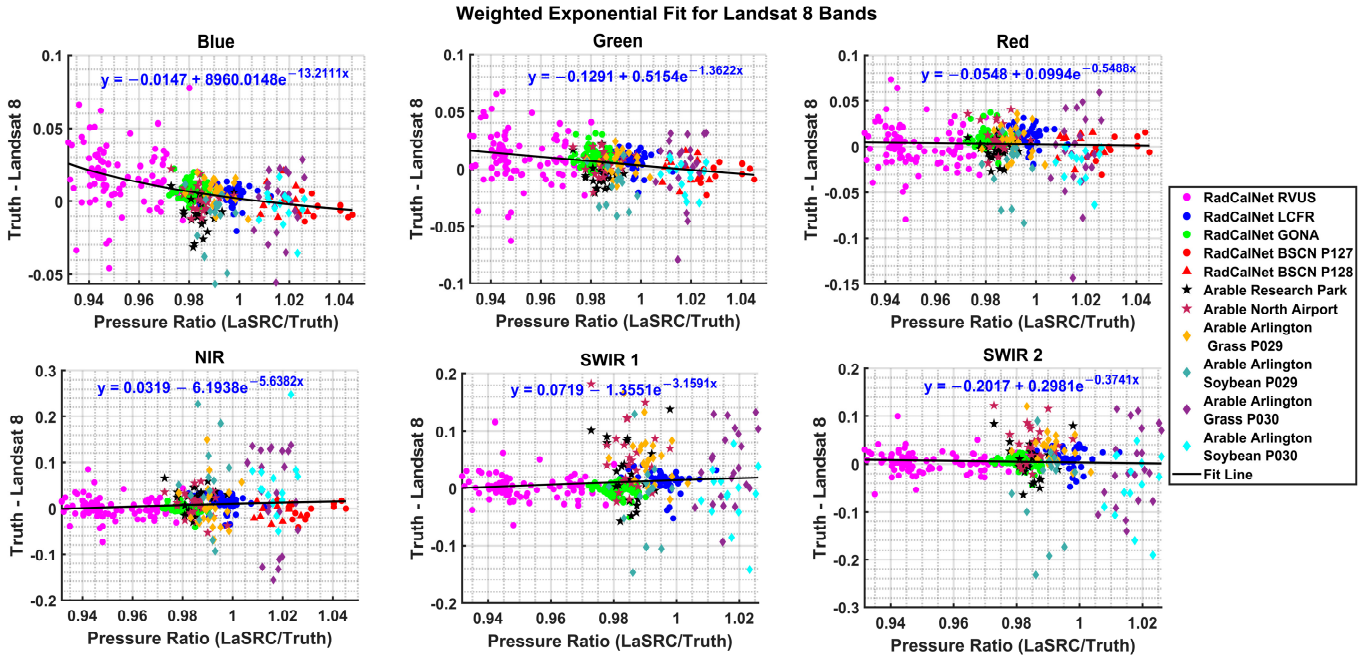


Figure 17. Weighted exponential with constant term fit for surface reflectance difference vs. pressure ratio for blue, green, red, NIR, SWIR 1, and SWIR 2 bands of Landsat 8.

Table 5. F-statistic and its *p*-value for exponential with the constant model for seven Landsat 8 surface reflectance bands.

Landsat 8 Bands	F-Statistic	*p*-Value	Significance at $\alpha = 0.01$
Coastal Aerosol	124	1.79×10^{-41}	Significant
Blue	97.6	1.68×10^{-20}	Significant
Green	15.7	3.02×10^{-7}	Significant
Red	0.311	0.733	Not significant
NIR	1.46	0.234	Not significant
SWIR 1	2.12	0.122	Not significant
SWIR 2	0.376	0.687	Not significant

The F-statistic and its associated *p*-value are presented in Table 5 and show that the pressure-related discrepancy is statistically significant at the 1% significance level [56] for coastal aerosol, blue, and green bands. However, for the red, NIR, SWIR 1, and SWIR 2 bands, the model is statistically not significant at the same significance level, which aligns with the earlier visual assessment.

Equation (11) represents the exponential correction model for surface reflectance difference (SR_{diff}), and Equation (12) gives the new (corrected) surface reflectance (SR_{new}) after applying the exponential correction model to the old (uncorrected) surface reflectance (SR_{old}) of Landsat 8. The coefficients of the correction model for coastal aerosol, blue, and green bands are tabulated in Table 6.

$$SR_{diff} = a + b \times e^{c \times \frac{LaSRC\ Pressure}{Ground\ Truth\ Pressure}} \quad (11)$$

$$SR_{new} = SR_{old} + a + b \times e^{c \times \frac{LaSRC\ Pressure}{Ground\ Truth\ Pressure}} \quad (12)$$

Table 6. Coefficients of the exponential correction model for coastal aerosol, blue and green bands of Landsat 8.

Landsat 8 Bands	a	b	c
Coastal Aerosol	−0.0555	83.5869	−7.2943
Blue	−0.0147	8960.0148	−13.2111
Green	−0.1291	0.5154	−1.3622

Figure 18 shows 1-to-1 plots before and after the Landsat 8 surface reflectance correction for coastal aerosol, blue, and green bands. The regression line is closer to the 1-to-1 line for all the bands after correction, showing improvement in the Landsat 8 Level 2 products. The most impacted sites due to the surface pressure differences, as can be seen from the 1-to-1 plot, are RVUS and BSCN, and the improvements are visible for these sites in the plots after correction.

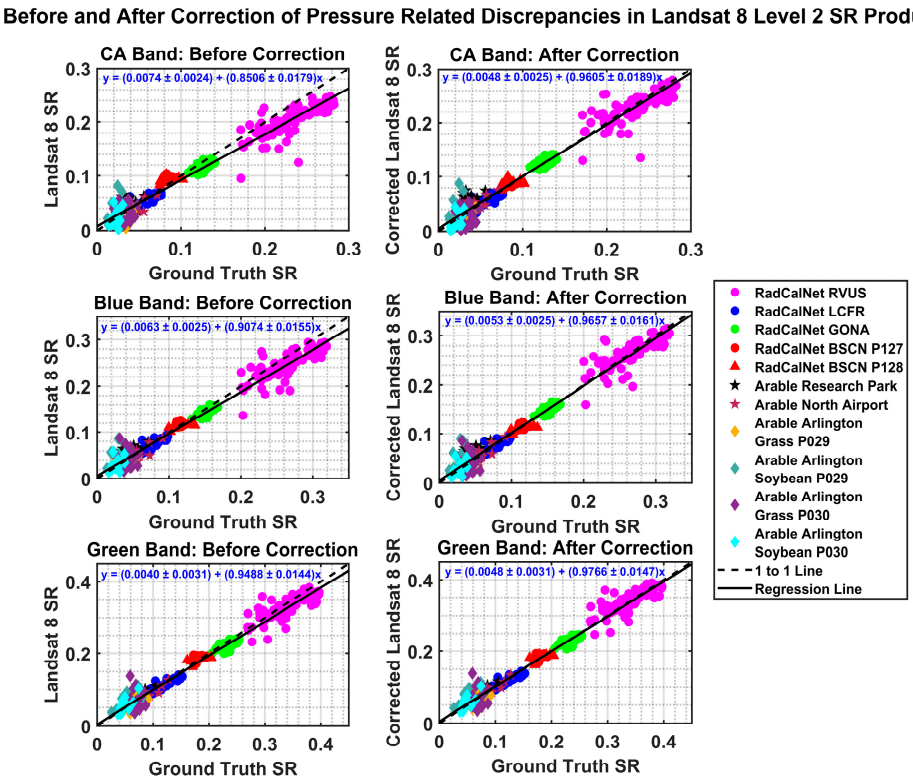


Figure 18. The 1-to-1 plots before and after correction of Landsat 8 Level 2 products for coastal aerosol, blue, and green bands.

The evaluation metrics, root mean square deviation (RMSD), mean error (ME), and mean absolute error (MAE) for the modeling datasets for the coastal aerosol, blue, and

green bands are presented in Table 7. All the evaluation metrics show improvement after correction for all three bands, with a decrement in errors. For example, before correction, the mean errors for the coastal aerosol, blue, and green bands were 0.0087, 0.0057, and 0.0054 reflectance units, respectively. After correction, they decreased to −0.0005, −0.0009, and −0.0005 reflectance units, respectively. This demonstrates that the correction reduced the mean error, bringing it closer to zero.

Table 7. Evaluation metrics—RMSD, ME, and MAE for the modeling dataset for the coastal aerosol, blue, and green bands of Landsat 8.

Landsat 8 Bands	Before Correction			After Correction		
	RMSD	ME	MAE	RMSD	ME	MAE
Coastal Aerosol	0.0203	0.0087	0.0145	0.0149	−0.0005	0.0101
Blue	0.0169	0.0057	0.0120	0.0145	−0.0009	0.0095
Green	0.0172	0.0054	0.0128	0.0158	−0.0005	0.0111

4.7. Validation

The selected models were validated using the 2024 RadCalNet dataset, as it represented the most recent observations and captured the pressure-related discrepancies in LaSRC most prominently. Figure 19 shows the performance of the models in the validation dataset. The regression line is closer to the 1-to-1 line for the coastal aerosol and blue band, whereas for the green band, the regression line deviated slightly away from the 1-to-1 line after the correction. As shown in Figure 19 (bottom left chart), the surface reflectance for the green band exhibited only a minor discrepancy. Therefore, when the model attempted to correct this slight deviation, it resulted in an undercorrection.

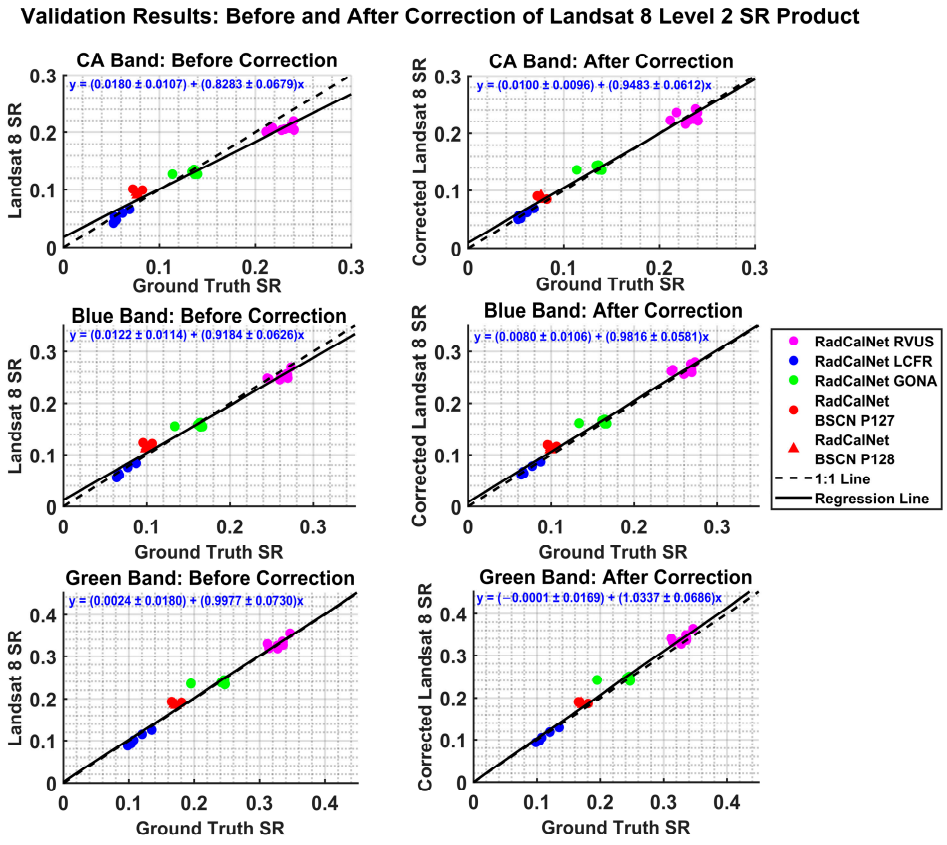


Figure 19. Validation results for the coastal aerosol, blue, and green bands of Landsat 8 using RadCalNet data of 2024.

Table 8 shows three evaluation metrics: RMSD, ME, and MAE for coastal aerosol, blue, and green bands of Landsat 8 before and after applying the correction. The statistics reveal that the errors for the most impacted sites due to the pressure-related discrepancies, RVUS and BSCN, were decreased for the coastal aerosol and blue band. For example, the mean error of the coastal aerosol band for the RVUS site decreased up to two reflectance units, from 0.0226 to 0.0029. Similarly, for the blue band, the mean error decreased from 0.0095 to −0.0032. For the BSCN sites, the mean error for the coastal aerosol band decreased up to one unit of reflectance, and for the blue band, the correction was up to half a unit of reflectance. For the green band, the correction had a smaller impact due to the lesser effects of aerosol on this channel, except for the BSCN Path 127, where a noticeable improvement in error is seen.

Table 8. Evaluation metrics—RMSD, ME, and MAE before and after correction of Landsat 8 surface reflectance for the validation dataset for coastal aerosol, blue, and green bands.

Landsat 8 Bands	RadCalNet Sites	RMSD	ME	MAE
Coastal Aerosol Band (Before Correction)	RVUS	0.0241	0.0226	0.0226
	LCFR	0.0060	0.0049	0.0049
	GONA	0.0086	0.0022	0.0067
	BSCN P127	0.0235	−0.0228	0.0228
	BSCN P128	0.0162	−0.0159	0.0159
	All Sites Combined	0.0173	0.0061	0.0140
Coastal Aerosol Band (After Correction)	RVUS	0.0122	0.0029	0.0111
	LCFR	0.0022	0.0006	0.0017
	GONA	0.0113	−0.0075	0.0089
	BSCN P127	0.0129	−0.0103	0.0103
	BSCN P128	0.0115	−0.0110	0.0110
	All Sites Combined	0.0106	−0.0027	0.0084
Blue Band (Before Correction)	RVUS	0.0123	0.0095	0.0103
	LCFR	0.0051	0.0044	0.0044
	GONA	0.0110	0.0007	0.0081
	BSCN P127	0.0228	−0.0219	0.0219
	BSCN P128	0.0148	−0.0147	0.0147
	All Sites Combined	0.0124	0.0013	0.0098
Blue Band (After Correction)	RVUS	0.0104	−0.0032	0.0090
	LCFR	0.0020	0.0012	0.0017
	GONA	0.0124	−0.0056	0.0088
	BSCN P127	0.0185	−0.0171	0.0171
	BSCN P128	0.0134	−0.0132	0.0132
	All Sites Combined	0.0111	−0.0050	0.0084
Green Band (Before Correction)	RVUS	0.0086	−0.0014	0.0067
	LCFR	0.0087	0.0084	0.0084
	GONA	0.0183	−0.0007	0.0127
	BSCN P127	0.0214	−0.0196	0.0196
	BSCN P128	0.0154	−0.0151	0.0151
	All Sites Combined	0.0138	−0.0019	0.0105
Green Band (After Correction)	RVUS	0.0147	−0.0114	0.0115
	LCFR	0.0046	0.0042	0.0042
	GONA	0.0196	−0.0071	0.0119
	BSCN P127	0.0186	−0.0159	0.0159
	BSCN P128	0.0155	−0.0152	0.0152
	All Sites Combined	0.0152	−0.0076	0.0107

5. Discussion

5.1. Impact of Inaccurate Estimation of Surface Pressure on Landsat 8 Surface Reflectance Discrepancies

This study finds significant discrepancies in Landsat 8 L2C2 surface reflectance products, particularly in the shorter wavelength bands. While previous studies by Pinto et al. [11] and Badawi et al. [12] have attributed these discrepancies to challenges in accurately estimating aerosol concentrations, they have not fully explored how aerosol estimation within the LaSRC framework might contribute to these errors. In contrast, our study reveals that the root cause of these discrepancies lies in the inaccurate estimation of surface pressure for the pixels, specifically, the application of a single scene center surface pressure value across the entire scene.

Through statistical tests, it was found that the pressure-related discrepancies affected three shorter wavelength bands of Landsat 8: coastal aerosol, blue, and green bands. To address this issue, an exponential correction model was developed that corrected the surface reflectance values based on pressure discrepancies. The application of this model led to marked improvements in the accuracy metrics, particularly at sites experiencing substantial pressure differences due to varying elevations.

5.2. Implications and Applications of the Findings

The developed correction model should be applied following the extraction of LaSRC-derived surface reflectance for Landsat 8 imagery. It is intended for applications that demand high reflectance accuracy within a defined flat ROI, especially for scenes containing complex terrains such as the valleys and elevated regions (like RVUS) outside the ROI. The correction is especially important for dark targets, which naturally exhibit low reflectance and are more vulnerable to errors arising from inaccurate surface pressure estimation. These ROIs, when prevalent in such scenes, are often the most affected by pressure-related discrepancies, potentially undermining the reliability of subsequent analyses. In such cases, the application of this correction model can significantly enhance the accuracy of reflectance-based assessments.

The correction procedure involves three main steps. First, extract the LaSRC-derived surface reflectance for the area of interest. Next, obtain the surface pressure values computed by LaSRC, following the procedures outlined in Methodology Section 3.1.2. Finally, acquire the ground truth surface pressure data and apply the correction using Equation (12).

The corrected surface reflectance can be used in various downstream applications. As the coastal aerosol band can be used to monitor chlorophyll concentrations from phytoplankton, algae blooms, and suspended sediments in coastal regions [57,58], with the correction applied, more reliable water quality assessments and informed coastal management can be achieved. The corrected blue band can enhance the accuracy of applications such as bathymetric mapping [59], differentiation between soil and vegetation, and discrimination of deciduous and coniferous vegetation types [60]. Finally, like the other two bands, corrections in the green band also enable more precise monitoring of vegetation growth and health.

5.3. Limitations and Future Research Directions

The proposed correction model represents a short-term, empirical workaround rather than a long-term, permanent solution. The model was developed by fitting residuals using data from the available ground truth sites. These sites represented a mix of dark and bright targets with diverse atmospheric and topographic conditions. In the future, researchers can add more ground truth sites, if available, which will help the model further capture and expand the environmental variability.

Furthermore, the model's validation was performed by splitting the available dataset rather than employing an independent, external validation dataset. Given the current ground truth data limitations, this approach may hinder the generalizability of the results. However, it should be noted that true ground truth data for surface reflectance is a very scarce and difficult-to-obtain resource. Future work should aim to validate the model with more variable ground-truth datasets if available.

Additionally, key atmospheric parameters such as atmospheric intrinsic reflectance, atmospheric spherical albedo, and total atmospheric transmission are influenced by both surface pressure and aerosol concentrations, as demonstrated in Equation (1). During this study, an effort was made to assess the impact of aerosol concentrations on the surface reflectance discrepancies. However, due to limitations in our capability of retrieving actual AOD values from the LaSRC outputs, we were unable to fully separate the influence of aerosols from that of surface pressure. Further research could aim to separate and quantify these influences, thereby providing a more thorough understanding of their respective contributions to atmospheric correction uncertainty.

Like surface pressure, the LaSRC algorithm applies the scene center values of ozone and water vapor to all pixels in a scene. The present study focused exclusively on assessing the impact of pressure discrepancies on surface reflectance products, as it was the primary contributor in the shorter wavelength bands. Hence, the potential effects of using uniform ozone and water vapor values were not investigated. This represents another potential limitation that might need future researchers to examine the individual and combined impacts of inaccurately estimated surface pressure, ozone, and water vapor on surface reflectance products.

5.4. Long-Term Fix to the Problem

The correction model proposed in this study serves as a short-term, empirical solution to mitigate inaccuracies in surface reflectance caused by the use of a single, scene center surface pressure value in the LaSRC algorithm. However, for a more robust and long-term solution, implementing surface pressure calculations at finer spatial resolutions will be essential. In this regard, the integration of high-resolution digital elevation models (DEMs) with sea-level pressure data from MODIS Terra ancillary information could facilitate more accurate, pixel-level surface pressure estimates across entire scenes.

This approach is technically feasible, as demonstrated by the current LaSRC retrieval of AOD, which is already retrieved over localized 3×3 pixel windows. This indicates that finer-scale processing is both computationally and operationally viable within the algorithm's existing framework. Moreover, the algorithm already incorporates dynamic atmospheric inputs such as ozone and water vapor from MODIS Terra in near real-time. Extending this capability to include sea-level pressure, used in conjunction with elevation data to derive surface pressure, would align with the already existing architecture and processing workflow.

6. Conclusions

This study reveals that the discrepancies observed in the shorter wavelength bands of Landsat 8 surface reflectance are primarily due to the inaccurate estimation of surface pressure, specifically, the application of a single, scene center surface pressure value across the entire scene pixels.

For accurate correction of the atmospheric effects in the images captured by EO satellites, it is imperative to have accurate input of atmospheric variables in the physics-based atmospheric correction algorithm. One of the atmospheric variables used in LaSRC is surface pressure, which plays a key role in the calculation of intrinsic atmospheric

reflectance, total atmospheric transmission, spherical albedo, gaseous transmission, and Rayleigh scattering reflectance. However, in LaSRC, elevation-based surface pressure is used instead of real surface pressure. Furthermore, the elevation-based pressure is also scene-centered, derived from a coarse resolution (0.05-degree) DEM file, which results in the use of a single surface pressure value for the entire scene pixels. Additionally, in the calculation of the scene center surface pressure, the algorithm assumes a fixed sea-level pressure of 1013 hPa without incorporating real-time meteorological variations. All of this has led to the inaccurate estimation of surface pressure within LaSRC, thereby leading to discrepancies in surface reflectance products.

The impacts of the pressure-related inaccuracies were assessed through the comparison of Landsat 8 SR products with in situ automated measurements from RadCalNet and Arable Mark 2 sensors. The largest discrepancies were observed in the coastal aerosol and blue bands, with the magnitude of discrepancies larger for regions with greater elevation differences between the study area and the Landsat 8 scene center. This effect was particularly visible in landscapes with varied topography, such as RVUS, where the scene center was positioned on elevated terrain while the study area was at a lower altitude. The same effect was observed at BSCN, where Landsat 8 scenes from different WRS-2 paths for the same study area had different surface reflectance differences. Path 127 scenes, having the greater elevation difference, hence the larger surface pressure difference, had higher surface reflectance differences compared to Path 128 scenes.

To mitigate these errors, an exponential correction model was developed to adjust surface reflectance based on pressure discrepancies. The correction model effectively reduced errors in the most impacted sites, particularly RVUS and BSCN, for the coastal aerosol and blue bands of Landsat 8. At RVUS, the mean error in the coastal aerosol band decreased from 0.0226 to 0.0029 (an improvement of approximately two units of reflectance), which is significant for darker vegetative and water targets. In the blue band, the mean error decreased from 0.0095 to -0.0032, which is more than half a unit of reflectance. Similarly, at BSCN, the mean error decreased by approximately one reflectance unit for the coastal aerosol band and half a reflectance unit for the blue band. However, for the green band, improvements were much smaller due to the minimal effects of aerosol on this band. In general, these results demonstrate the effectiveness of the correction model in minimizing discrepancies caused by the use of a single scene center surface pressure for the entire scene pixels.

Overall, this study underscores the significance of surface pressure estimation within LaSRC and highlights the need for better estimation of surface pressure to improve surface reflectance accuracy. Though the short-term solution is proposed in this paper for the Landsat 8 Level 2 Collection 2 products, for the long term, implementing surface pressure calculations at finer spatial resolutions will be essential. In this regard, integrating high-resolution digital elevation models (DEMs) with sea-level pressure data from MODIS Terra ancillary information could facilitate more accurate, pixel-level surface pressure estimates across entire scenes. Additionally, the effects of the use of the scene center value of other atmospheric variables, such as water vapor and ozone content, on surface reflectance accuracy warrant further research and investigation.

Author Contributions: Conceptualization, S.A. and L.L.; methodology, S.A. and L.L.; software, S.A. and L.L.; validation, S.A. and L.L.; formal analysis, S.A. and L.L.; investigation, S.A. and L.L.; resources, L.L.; data curation, S.A., L.L. and D.S.P.; writing—original draft preparation, S.A.; writing—review and editing, S.A., L.L. and D.S.P.; visualization, S.A.; supervision, L.L.; project administration, L.L.; funding acquisition, L.L. All authors have read and agreed to the published version of the manuscript.

Funding: This research was funded by USGS EROS, grant number SA2500150.

Data Availability Statement: The RadCalNet data are available through the RadCalNet portal (www.radcalnet.org, accessed on 10 January 2025). Landsat 8 data are provided by the U.S. Geological Survey and accessible via USGS Earth Explorer at https://earthexplorer.usgs.gov (accessed on 20 July 2024). Landsat Collection 2 atmospheric auxiliary data are available at the U.S. Geological Survey website: https://www.usgs.gov/landsat-missions/landsat-collection-2-atmospheric-auxiliary-data (accessed on 20 July 2024).

Acknowledgments: The author is extremely grateful to USGS EROS for providing the current operational version of the LaSRC for analysis purposes. The author also expresses profound and heartfelt gratitude to Larry Leigh for continuous motivation, guidance, and support throughout the project. The author would also like to thank Jeffrey S. Czapla-Myers (University of Arizona) for providing 1 nm hyperspectral surface reflectance data of Railroad Valley Playa, which was used to assess the need for spectral interpolation for RadCalNet datasets. Special appreciation is extended to all members of the Image Processing Laboratory for their valuable feedback and suggestions during weekly meetings. Finally, the author extends heartfelt thanks to family members for their constant encouragement and unwavering support.

Conflicts of Interest: The authors declare no conflicts of interest.

Appendix A

The table for the comparison of different methods of spectral interpolation is presented in Table A1.

Table A1. Comparison of the differences in five methods of band integration (band averaged 10 nm, linear, makima, spline, and PCHIP interpolation) to Landsat 8. The data are in reflectance units.

Bands	Band-Integrated Band Averaged (10 nm)	Band-Integrated Linear (1 nm)	Band-Integrated Makima (1 nm)	Band-Integrated Spline (1 nm)	Band-Integrated PCHIP (1 nm)
Coastal Aerosol	0.001198	0.000050	−0.000009	−0.000007	−0.000010
Blue	0.001775	−0.000006	0.000004	0.000004	0.000004
Green	0.000879	0.000174	0.000057	0.000058	0.000058
Red	0.000033	0.000007	0.000011	0.000005	0.000011
NIR	−0.000012	0.000006	0.000003	0.000003	0.000003
SWIR 1	0.000002	0.000007	0.000003	0.000003	0.000003
SWIR 2	0.000037	0.000065	0.000025	0.000023	0.000025

Different types of weighted fits used to model surface reflectance discrepancies in the coastal aerosol band, resulting from inaccurate surface pressure estimation within LaSRC, are presented in Figures A1–A7.

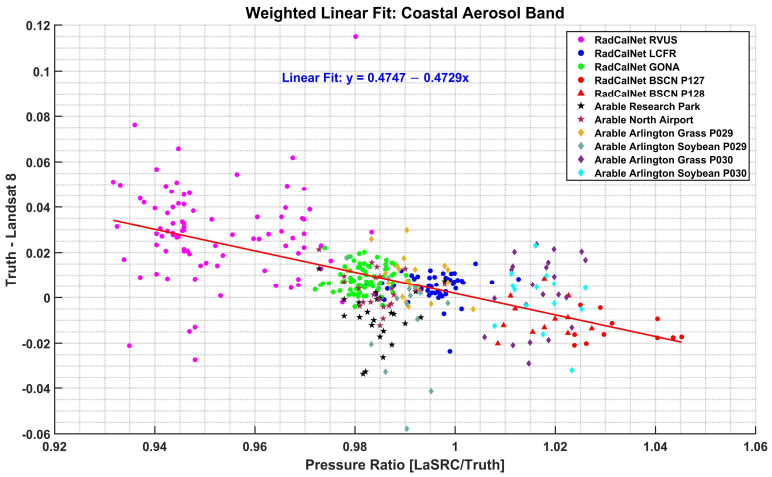


Figure A1. Weighted linear fit for surface reflectance difference vs. surface pressure ratio for the coastal aerosol band of Landsat 8.

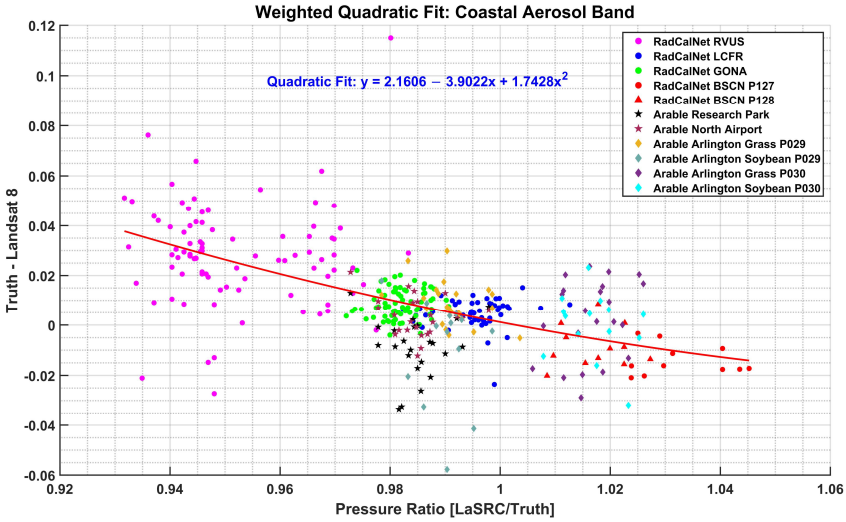


Figure A2. Weighted quadratic fit for surface reflectance difference vs. surface pressure ratio for the coastal aerosol band of Landsat 8.

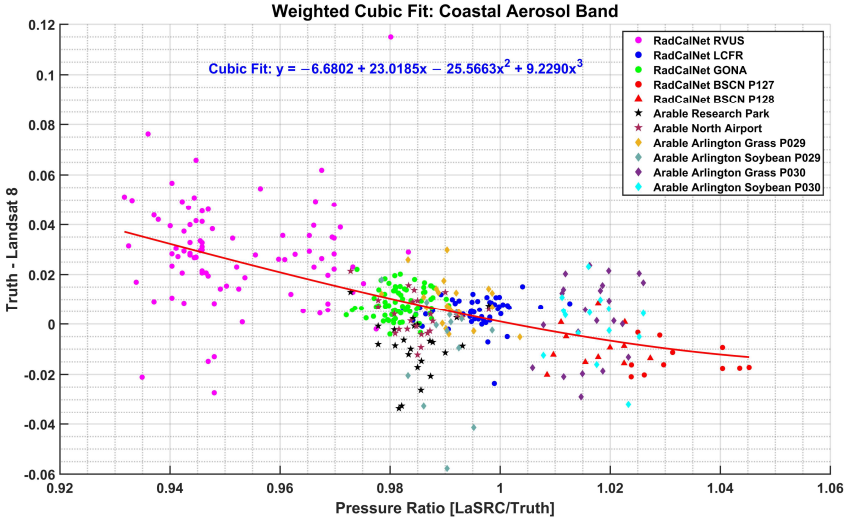


Figure A3. Weighted cubic fit for surface reflectance difference vs. surface pressure ratio for the coastal aerosol band of Landsat 8.

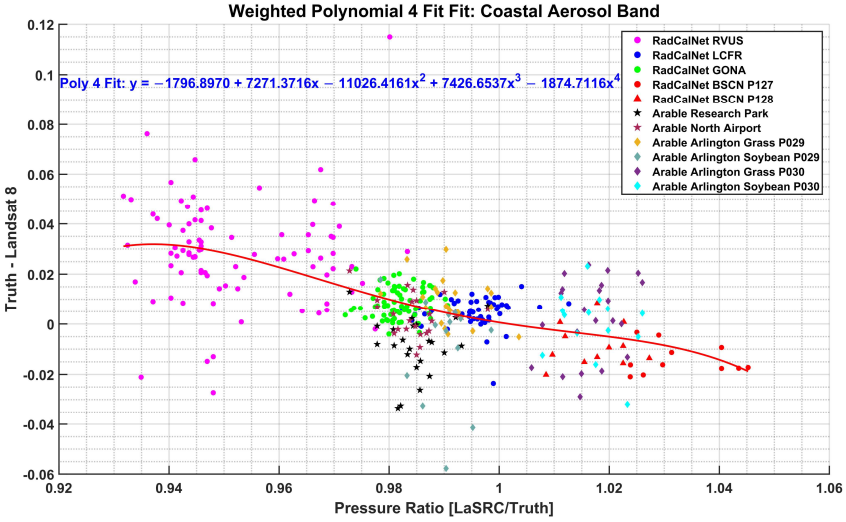


Figure A4. Weighted polynomial four fit for surface reflectance difference vs. surface pressure ratio for the coastal aerosol band of Landsat 8.

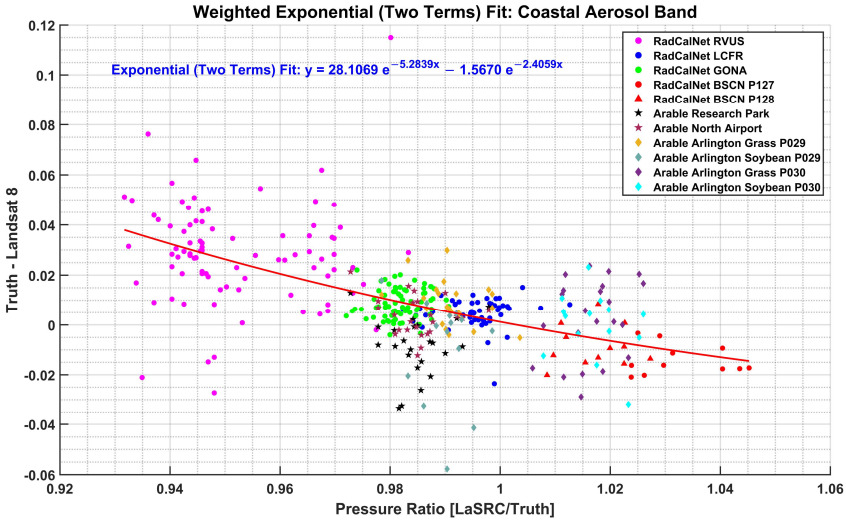


Figure A5. Weighted two exponential terms fit for surface reflectance difference vs. surface pressure ratio for the coastal aerosol band of Landsat 8.

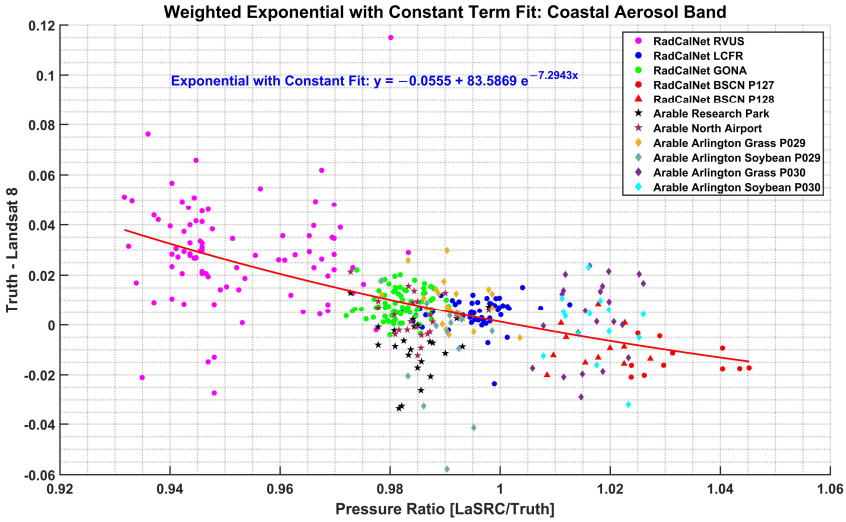


Figure A6. Weighted exponential with constant term fit for surface reflectance difference vs. surface pressure ratio for the coastal aerosol band of Landsat 8.

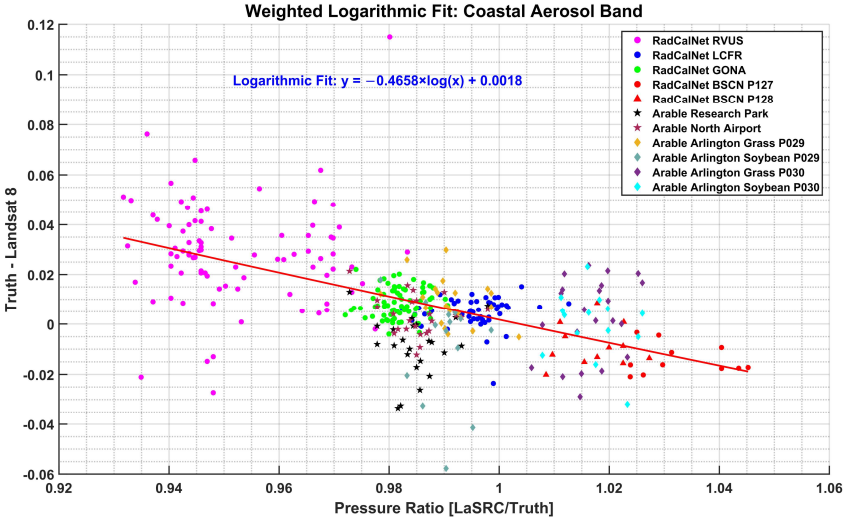


Figure A7. Weighted logarithmic fit for surface reflectance difference vs. surface pressure ratio for the coastal aerosol band of Landsat 8.

References

1. Eyre, J.; Bell, W.; Cotton, J.; English, S.; Forsythe, M.; Healy, S.; Pavelin, E. Assimilation of satellite data in numerical weather prediction. Part II: Recent years. *Q. J. R. Meteorol. Soc.* **2022**, *148*, 521–556. [CrossRef]
2. Maimaitijiang, M.; Sagan, V.; Sidike, P.; Daloye, A.M.; Erkbol, H.; Fritschi, F.B. Crop Monitoring Using Satellite/UAV Data Fusion and Machine Learning. *Remote Sens.* **2020**, *12*, 1357. [CrossRef]
3. Hatfield, P.; Pinter, P., Jr. Remote sensing for crop protection. *Crop Prot.* **1993**, *12*, 403–413. [CrossRef]
4. Wooster, M.J.; Roberts, G.J.; Giglio, L.; Roy, D.P.; Freeborn, P.H.; Boschetti, L.; Justice, C.; Ichoku, C.; Schroeder, W.; Davies, D. Satellite remote sensing of active fires: History and current status, applications and future requirements. *Remote Sens. Environ.* **2021**, *267*, 112694. [CrossRef]
5. Poland, M.P.; Lopez, T.; Wright, R.; Pavolonis, M.J. Forecasting, detecting, and tracking volcanic eruptions from space. *Remote Sens. Earth Syst. Sci.* **2020**, *3*, 55–94. [CrossRef]
6. Martin, R.V. Satellite remote sensing of surface air quality. *Atmos. Environ.* **2008**, *42*, 7823–7843. [CrossRef]
7. U.S. Geological Survey. *Landsat 8-9 Operational Land Imager (OLI)—Thermal Infrared Sensor (TIRS) Collection 2 Level 1 (L1) Data Format Control Book (DFCB)*; U.S. Geological Survey: Reston, VA, USA, 2020.
8. U.S. Geological Survey. *Landsat 8-9 Operational Land Imager (OLI)—Thermal Infrared Sensor (TIRS) Collection 2 (C2) Level 2 (L2) Data Format Control Book (DFCB)*; U.S. Geological Survey: Reston, VA, USA, 2022.
9. Vermote, E.; Justice, C.; Claverie, M.; Franch, B. Preliminary analysis of the performance of the Landsat 8/OLI land surface reflectance product. *Remote Sens. Environ.* **2016**, *185*, 46–56. [CrossRef]
10. Wu, Z.; Snyder, G.; Vadnais, C.; Arora, R.; Babcock, M.; Stensaas, G.; Doucette, P.; Newman, T. User needs for future Landsat missions. *Remote Sens. Environ.* **2019**, *231*, 111214. [CrossRef]
11. Teixeira Pinto, C.; Jing, X.; Leigh, L. Evaluation Analysis of Landsat Level-1 and Level-2 Data Products Using In Situ Measurements. *Remote Sens.* **2020**, *12*, 2597. [CrossRef]
12. Badawi, M.; Helder, D.; Leigh, L.; Jing, X. Methods for Earth-Observing Satellite Surface Reflectance Validation. *Remote Sens.* **2019**, *11*, 1543. [CrossRef]
13. U.S. Geological Survey. *Landsat Next 2024-3005*; U.S. Geological Survey: Reston, VA, USA, 2024; p. 2.
14. Nazeer, M.; Ilori, C.O.; Bilal, M.; Nichol, J.E.; Wu, W.; Qiu, Z.; Gayene, B.K. Evaluation of atmospheric correction methods for low to high resolutions satellite remote sensing data. *Atmos. Res.* **2021**, *249*, 105308. [CrossRef]
15. Kotchenova, S.Y.; Vermote, E.F.; Matarrese, R.; Klemm, F.J., Jr. Validation of a vector version of the 6S radiative transfer code for atmospheric correction of satellite data. Part I: Path radiance. *Appl. Opt.* **2006**, *45*, 6762–6774. [CrossRef]
16. Kotchenova, S.Y.; Vermote, E.F. Validation of a vector version of the 6S radiative transfer code for atmospheric correction of satellite data. Part II. Homogeneous Lambertian and anisotropic surfaces. *Appl. Opt.* **2007**, *46*, 4455–4464. [CrossRef]
17. Tanré, D.; Deroo, C.; Duhaut, P.; Herman, M.; Morcrette, J.; Perbos, J.; Deschamps, P. Technical note Description of a computer code to simulate the satellite signal in the solar spectrum: The 5S code. *Int. J. Remote Sens.* **1990**, *11*, 659–668. [CrossRef]
18. Berk, A.; Anderson, G.P.; Acharya, P.K.; Bernstein, L.S.; Muratov, L.; Lee, J.; Fox, M.; Adler-Golden, S.M.; Chetwynd, J.H., Jr.; Hoke, M.L. MODTRAN5: 2006 update. In Proceedings of the Algorithms and Technologies for Multispectral, Hyperspectral, and Ultraspectral Imagery XII, Orlando, FL, USA, 8 May 2006; pp. 508–515.
19. Kneizys, F.X. *Users Guide to LOWTRAN 7*; Air Force Geophysics Laboratory: Bedford, MA, USA, 1988; Volume 88.
20. Masek, J.G.; Vermote, E.F.; Saleous, N.E.; Wolfe, R.; Hall, F.G.; Huemmrich, K.F.; Gao, F.; Kutler, J.; Lim, T.K. A Landsat Surface Reflectance Dataset for North America, 1990–2000. *IEEE Geosci. Remote Sens. Lett.* **2006**, *3*, 68–72. [CrossRef]
21. Wilson, R.T. Py6S: A Python interface to the 6S radiative transfer model. *Comput. Geosci.* **2013**, *51*, 166–171. [CrossRef]
22. Frantz, D. FORCE—Landsat + Sentinel-2 Analysis Ready Data and Beyond. *Remote Sens.* **2019**, *11*, 1124. [CrossRef]
23. Sterckx, S.; Knaeps, E.; Adriaensen, S.; Reusen, I.; De Keukelaere, L.; Hunter, P.; Giardino, C.; Odermatt, D. OPERA: An atmospheric correction for land and water. In Proceedings of the Sentinel-3 for Science Workshop, Venice, Italy, 2–5 June 2015; pp. 3–6.
24. Anderson, G.P.; Felde, G.W.; Hoke, M.L.; Ratkowski, A.J.; Cooley, T.W.; Chetwynd, J.H., Jr.; Gardner, J.; Adler-Golden, S.M.; Matthew, M.W.; Berk, A. MODTRAN4-based atmospheric correction algorithm: FLAASH (fast line-of-sight atmospheric analysis of spectral hypercubes). In Proceedings of the Algorithms and Technologies for Multispectral, Hyperspectral, and Ultraspectral Imagery VIII, Orlando, FL, USA, 2 August 2002; pp. 65–71.
25. Nazeer, M.; Nichol, J.E.; Yung, Y.K. Evaluation of atmospheric correction models and Landsat surface reflectance product in an urban coastal environment. *Int. J. Remote Sens.* **2014**, *35*, 6271–6291. [CrossRef]
26. KC, M.; Leigh, L.; Pinto, C.T.; Kaewmanee, M. Method of Validating Satellite Surface Reflectance Product Using Empirical Line Method. *Remote Sens.* **2023**, *15*, 2240. [CrossRef]
27. Chavez, P.S., Jr. An improved dark-object subtraction technique for atmospheric scattering correction of multispectral data. *Remote Sens. Environ.* **1988**, *24*, 459–479. [CrossRef]
28. Richter, R. A spatially adaptive fast atmospheric correction algorithm. *Int. J. Remote Sens.* **1996**, *17*, 1201–1214. [CrossRef]

29. Hsu, N.C.; Tsay, S.C.; King, M.D.; Herman, J.R. Deep Blue Retrievals of Asian Aerosol Properties During ACE-Asia. *IEEE Trans. Geosci. Remote Sens.* **2006**, *44*, 3180–3195. [CrossRef]
30. Hsu, N.C.; Jeong, M.J.; Bettenhausen, C.; Sayer, A.M.; Hansell, R.; Seftor, C.S.; Huang, J.; Tsay, S.C. Enhanced Deep Blue aerosol retrieval algorithm: The second generation. *J. Geophys. Res. Atmos.* **2013**, *118*, 9296–9315. [CrossRef]
31. Kaufman, Y.J.; Wald, A.E.; Remer, L.A.; Gao, B.C.; Li, R.R.; Flynn, L. The MODIS 2.1-/spl mu/m channel-correlation with visible reflectance for use in remote sensing of aerosol. *IEEE Trans. Geosci. Remote Sens.* **1997**, *35*, 1286–1298. [CrossRef]
32. Tanré, D.; Kaufman, Y.; Herman, M.; Mattoo, S. Remote sensing of aerosol properties over oceans using the MODIS/EOS spectral radiances. *J. Geophys. Res. Atmos.* **1997**, *102*, 16971–16988. [CrossRef]
33. Remer, L.A.; Levy, R.C.; Mattoo, S.; Tanré, D.; Gupta, P.; Shi, Y.; Sawyer, V.; Munchak, L.A.; Zhou, Y.; Kim, M.; et al. The Dark Target Algorithm for Observing the Global Aerosol System: Past, Present, and Future. *Remote Sens.* **2020**, *12*, 2900. [CrossRef]
34. Bouvet, M.; Thome, K.; Berthelot, B.; Bialek, A.; Czapla-Myers, J.; Fox, N.; Goryl, P.; Henry, P.; Ma, L.; Marcq, S.; et al. RadCalNet: A Radiometric Calibration Network for Earth Observing Imagers Operating in the Visible to Shortwave Infrared Spectral Range. *Remote Sens.* **2019**, *11*, 2401. [CrossRef]
35. RadCalNet. Available online: https://www.radcalnet.org (accessed on 10 December 2024).
36. Czapla-Myers, J. *RadCalNet Site Description, CEOS Reference: QA4EO-WGCV-RadCalNet-RVUS-Q-v2*; University of Arizona: Tucson, AZ, USA, 2022.
37. Shrestha, M.; Helder, D.; Christopherson, J. DLR Earth Sensing Imaging Spectrometer (DESIS) Level 1 Product Evaluation Using RadCalNet Measurements. *Remote Sens.* **2021**, *13*, 2420. [CrossRef]
38. Landier, L. *RadCalNet Site Description, CEOS Reference: QA4EO-WGCV-RadCalNet-LCFR-Q-v3*; CNES, Physics for Optical Measurement Service: Belin, France, 2022.
39. Bialek, A.; Sinclair, M. *RadCalNet Site Description, CEOS Reference: QA4EO-WGCV-RadCalNet-GONA-Q-v2*; National Physical Laboratory: Hampton Road, UK, 2022.
40. Marcq, S.; Meygret, A.; Bouvet, M.; Fox, N.; Greenwell, C.; Scott, B.; Berthelot, B.; Besson, B.; Guilleminot, N.; Damiri, B. New RadCalNet site at Gobabeb, Namibia: Installation of the instrumentation and first satellite calibration results. In Proceedings of the IGARSS 2018-2018 IEEE International Geoscience and Remote Sensing Symposium, Valencia, Spain, 22–27 July 2018; pp. 6444–6447.
41. Ma, L. *RadCalNet Site Description, CEOS Reference: QA4EO-WGCV-RadCalNet-BSCN-Q-v3*; Aerospace Information Research Institute, Chinese Academy of Science: Beijing, China, 2022.
42. Image Processing Lab. Available online: https://www.sdstate.edu/mccomish-electrical-engineering-computer-science/image-processing-lab (accessed on 15 December 2024).
43. Pathiranage, D.S.; Leigh, L.; Pinto, C.T. Evaluation of Low-Cost Radiometer for Surface Reflectance Retrieval and Orbital Sensor's Validation. *Remote Sens.* **2023**, *15*, 2444. [CrossRef]
44. Kaufman, Y.J.; Sendra, C. Algorithm for automatic atmospheric corrections to visible and near-IR satellite imagery. *Int. J. Remote Sens.* **1988**, *9*, 1357–1381. [CrossRef]
45. Crawford, C.J.; Roy, D.P.; Arab, S.; Barnes, C.; Vermote, E.; Hulley, G.; Gerace, A.; Choate, M.; Engebretson, C.; Micijevic, E. The 50-year Landsat collection 2 archive. *Sci. Remote Sens.* **2023**, *8*, 100103. [CrossRef]
46. Arable Mark 2 Product Specifications. Available online: https://www.arable.com/wp-content/uploads/2021/10/Arable-Mark-2-w_-Solar-Product-Specifications-20_10.pdf (accessed on 15 December 2024).
47. Arable Mark 2 Measurements. Available online: https://www.arable.com/wp-content/uploads/2021/10/Arable-Mark-2-Measurements-21_05.pdf (accessed on 15 December 2024).
48. U.S. Geological Survey. *Landsat 8-9 Collection 2 (C2) Level 2 Science Product (L2SP) Guide*; U.S. Geological Survey: Reston, VA, USA, 2024.
49. Landsat Collection 2 Atmospheric Auxiliary Data. Available online: https://www.usgs.gov/landsat-missions/landsat-collection-2-atmospheric-auxiliary-data (accessed on 13 December 2024).
50. Vermote, E.F.; Tanré, D.; Deuze, J.L.; Herman, M.; Morcette, J.J. Second simulation of the satellite signal in the solar spectrum, 6S: An overview. *IEEE Trans. Geosci. Remote Sens.* **1997**, *35*, 675–686. [CrossRef]
51. Earth Resources Observation and Science (EROS) Center. *MODIS Fused, Collection 2 [Dataset]*; U.S. Geological Survey: Reston, VA, USA, 2021. [CrossRef]
52. Earth Resources Observation and Science (EROS) Center. *VIIRS, Collection 2 [Dataset]*; U.S. Geological Survey: Reston, VA, USA, 2023. [CrossRef]
53. Kaufman, Y.J.; Tanré, D.; Remer, L.A.; Vermote, E.F.; Chu, A.; Holben, B.N. Operational remote sensing of tropospheric aerosol over land from EOS moderate resolution imaging spectroradiometer. *J. Geophys. Res. Atmos.* **1997**, *102*, 17051–17067. [CrossRef]
54. Menne, M.J.; Noone, S.; Casey, N.W.; Dunn, R.H.; McNeill, S.; Kantor, D.; Thorne, P.W.; Orcutt, K.; Cunningham, S.; Risavi, N. *Global Historical Climatology Network-Hourly (GHCNh), Version 1*; NOAA National Centers for Environmental Information: New Orleans, LA, USA, 12–16 January 2025. [CrossRef]

55. U.S. Geological Survey. *Landsat 8-9 Calibration and Validation (Cal/Val) Algorithm Description Document (ADD)*; U.S. Geological Survey: Reston, VA, USA, 2021.
56. Ott, R.; Longnecker, M. *An Introduction to Statistical Methods and Data Analysis*; Cengage Learning Inc.: Boston, MA, USA, 2010; p. 687.
57. Concha, J.A.; Schott, J.R. Retrieval of color producing agents in Case 2 waters using Landsat 8. *Remote Sens. Environ.* **2016**, *185*, 95–107. [CrossRef]
58. Algae Bloom on Lake Erie. Available online: https://earthobservatory.nasa.gov/images/84125/algae-bloom-on-lake-erie (accessed on 10 April 2025).
59. Jagalingam, P.; Akshaya, B.; Hegde, A.V. Bathymetry mapping using Landsat 8 satellite imagery. *Procedia Eng.* **2015**, *116*, 560–566. [CrossRef]
60. What Are the Best Landsat Spectral Bands for Use in My Research? Available online: https://www.usgs.gov/faqs/what-are-best-landsat-spectral-bands-use-my-research (accessed on 11 April 2025).

Disclaimer/Publisher's Note: The statements, opinions and data contained in all publications are solely those of the individual author(s) and contributor(s) and not of MDPI and/or the editor(s). MDPI and/or the editor(s) disclaim responsibility for any injury to people or property resulting from any ideas, methods, instructions or products referred to in the content.